Contactless Dielectrophoresis towards Drug Screening and Microdevice Development for Cell Sorting

Elizabeth Ashcraft Savage Elvington

Thesis submitted to the faculty of the Virginia Polytechnic Institute and State University in partial fulfillment of the requirements for the degree of

Master of Science
In
Biomedical Engineering

Rafael V. Davalos
Eva M. Schmelz
Mark A. Stremler

May 28, 2013
Blacksburg, VA

Keywords: Dielectrophoresis, Drug screening, Cell sorting, Ovarian cancer

Contactless Dielectrophoresis towards Drug Screening and Microdevice Development for Cell Sorting

Elizabeth Ashcraft Savage Elvington

ABSTRACT

Firstly, this work demonstrates that contactless dielectrophoresis (cDEP) was useful to detect a reversal in the electrical phenotype of late-stage ovarian cancer cells to a profile similar to that of slow-growing early-stage ovarian epithelial cells after treatment with a non-toxic bioactive metabolite, sphingosine. Current chemotherapeutics are highly toxic to patients and can cause severe adverse side effects, so non-toxic treatments that could slow or reverse cancer growth would be advantageous. This is the first instance of cDEP for detecting induced changes in cell structure, showing its potential as a rapid, non-biomarker-based drug screening platform.

Specifically, low frequency contactless dielectrophoresis devices previously designed by Sano *et al* were used to extract the crossover frequency and specific membrane capacitance of early and late stage mouse ovarian surface epithelial (MOSE-E and MOSE-L) cells when untreated, treated with the anti-cancer sphingosine (So) metabolite and with a generally cancer-supporting sphingosine-1-phosphate (S1P) metabolite. The specific membrane capacitance of MOSE-L cells treated with So decreased and the normalized crossover frequency increased to levels matching MOSE-E cells.

Secondly, a new multilayer cDEP device featuring curved interdigitated electrode channels overlaying a straight sample channel for the purpose of cell sorting was designed, computationally modeled, fabricated, and tested. The goal of this design was to achieve continuous multi-stream sorting of cells, and preliminary testing demonstrated that prostate cancer PC3 cells were continuously deflected toward the top of the channel under an electric field, as predicted by the numerical model.

Acknowledgements

I would like to first thank Dr. Davalos, my advisor, for providing the opportunity for me to participate in this exciting work and for his unwavering support and guidance throughout. Many thanks to Dr. Schmelz for advising the biological portions of this thesis and for introducing me to perspectives distinct from those in my engineering background, and to Dr. Stremler for support and advice throughout my time here. Many thanks to the founding members of the cDEP group in the Bioelectromechanical Systems (BEMS) laboratory without whom this work would not have been possible. Specifically, I am grateful to Mike Sano, Alireza Salmanzadeh, and Andrea Rojas, who were generous mentors and colleagues. Many thanks to all my BEMS colleagues, especially Lisa Anders and Katie Prokop, for the general support and fun conversations. Thanks to undergraduate researchers Caitlan Swaffar, Lindsay Carr, and Karli Brittain for sharing their enthusiasm and friendship, and inspiring me to continue growing as a mentor. I would also like to acknowledge the financial support of the MultiSTEPS Interdisciplinary Graduate Education Program (IGEP) and NSF Emerging Frontiers in Research and Innovation (EFRI).

An impossibly large debt is owed to my parents Chris and Mary Anne Savage for teaching me long division during beach vacations, algebra as bedtime stories, heat transfer while boiling pasta, and more importantly, that while I am a great sinner, Christ is a great Savior. Words are not sufficient to express the blessing that the unconditional love and encouragement of my husband Jason are to me, and I am thankful for his willingness to walk through the ups and downs of graduate school alongside me. This work is dedicated to my family members and dear friends who have fought or are fighting cancer, especially my grandparents Mary & Ed Gibbs, aunt Karina Gibbs, grandfather Robert Savage, and my mother Mary Anne. Finally, to the One who heals both body and soul, “Blessed be the God and Father of our Lord Jesus Christ, who has blessed us in Christ…In him we have redemption through his blood, the forgiveness of our trespasses, according to the riches of his grace, which he lavished upon us.” Ephesians 1:3, 7-8

Table of Contents

List of Figures

bottom of the channel to achieve cell sorting. (c) Zig-zag electrode channels generate maxima of DEP force to support focusing of cells previously sorted upstream.

List of Tables

Chapter 1. Introduction

The National Cancer Institute estimates that about 41% of men and women will be diagnosed with some form of cancer during their lives [1] and that in 2012 over 1.6 million people were diagnosed, almost 580,000 of whom would die from the disease [2]. In particular, ovarian cancer is the fifth leading cause of cancer-related deaths in women but the most commonly lethal of all gynecological cancers [3-5]. In 2012, it was estimated that there were 22,280 new cases and 15,500 deaths due to ovarian cancer [2].

According to the National Cancer Institute, chemotherapy was administered to over 70% of patients with stage III or IV ovarian cancer during 1991-2002, and to over 50% of patients with stage I or II ovarian cancer during the same time span [6]. Current chemotherapy treatments are highly toxic and lead to severe adverse side effects in addition to a range of less drastic side effects. As reported by the National Cancer Institute, paclitaxel and carboplatin or cisplatin are the most commonly administered drugs to treat ovarian cancer [6]. Paclitaxel commonly causes neurotoxicity, while cisplatin induces nephrotoxicity, which thus limit the possible dose administered [6-8]. Because ovarian cancer is a genetically and histologically heterogeneous disease, the lack of common genetic markers hinders both cancer detection at earlier stages and the development of successful treatment options. Development of treatment regimens and detection techniques that do not rely upon the expression of specific genes or surface markers could ameliorate these challenges. A method for biomarker-independent treatment screening could contribute to successful treatment development and clinical evaluation of treatment efficacy towards personalized medicine.

Dielectrophoresis (DEP), the translational motion of polarizable particles in a non-uniform electric field, allows interrogation of biophysical properties of particles without requiring prior knowledge of surface biomarkers [9]. Cells may be suspended in a liquid medium and introduced to a microchamber in which the non-uniform electric field exists [10]. Based on differences between physical characteristics of cell populations, such as

size, shape, membrane roughness, cytoskeletal structure, nucleus to cytoplasm ratio, and cytoplasm conductivity, cell motion can be directed by tuning the frequency of the electric field.

Two methods of influencing the DEP response of cells include (1) altering the cell biophysics by means of a drug or other treatment, or (2) designing electrode and overall device geometry to produce specified spatial electric field gradients. These two methods will be explored in this work. Firstly, the effect of non-toxic bioactive metabolites on dielectric properties of ovarian cancer cells will be elucidated, and secondly, the design process for developing a new DEP-based microdevice will be demonstrated.

Chapter 2. Background & Significance

2.1 Sphingolipids for Treating Ovarian Cancer

The National Cancer Institute estimates that about 41% of men and women will be diagnosed with some form of cancer during their lives [1] and that in 2012 over 1.6 million people were diagnosed, almost 580,000 of whom would die from the disease [2]. Specifically, ovarian cancer is the most frequent cause of death from gynecological malignancies in women and the fifth leading cause of death from cancer in women [3, 4].

Current cancer treatments rely upon highly toxic doses of chemotherapeutics and can cause severe adverse side effects. In addition to achieving early detection, the development of less aggressive treatment options that at least partially reverse the aggressive phenotype of the disease to an earlier, more benign state and therefore may turn a deadly cancer into a chronic disease could be highly beneficial for patients. Toward this vision, orally administered complex sphingolipids have been administered to successfully suppress colon and breast cancer [11-15].

Sphingolipids are molecules that may be characterized by an 18 carbon chain with an alcohol-amino backbone [16], and are synthesized in the endoplasmic reticulum or ingjested from dietary sources [17]. The sphingolipid family of metabolites influences membrane biology and as lipid second messengers, sphingolipids modulate cellular homeostasis, as well as functions and responses to extracellular stimuli. Sphingolipids are involved in the regulation of cell growth, cell death, migration, angiogenesis, and metabolism, among many other cell functions [16, 18]. Dysregulation in metabolic pathways of sphingolipids can cause progression of some diseases, including cancer.[19, 20] The sphingolipid metabolites ceramide (Cer), sphingosine (So), and sphingosine-1-phosphate (S1P), can stimulate opposing cellular responses depending upon their relative levels in a cell, forming the so-called sphingolipid rheostat [21, 22]. In general, So and Cer are known as a death-promoting factors leading to apoptosis, inhibition of cell

growth, differentiation, migration, and angiogenesis [23] and thus could be considered tumor suppressors. Interestingly, sphingosine also can transport across membranes by diffusion due its amphipathic properties [16]. Cer is unable to diffuse across membranes and is spatially contained within organelles Cer also been associated with inflammation, [24] suggesting a tumor promoting effect. In contrast, S1P acts to support growth and survival of numerous cell types. As such, it has tumor-promoting effects, including inhibition of apoptosis and stimulation of angiogenesis, cell proliferation, differentiation, and migration [23],[21]. S1P is restricted to the membrane but can be exported by a lipid transporter. Elevated levels of S1P have been reported in ascites fluid of patients with ovarian cancer [25] and may promote the survival, adherence, and outgrowth of peritoneal metastases. Interestingly, therapies targeting S1P generation and signaling have led to a decreased tumor formation in mice [26].

2.2 Foundations of Dielectrophoresis (DEP)

Electrokinetic phenomena include effects such as electrophoresis, electro-osmotic flow, electrorotation, and dielectrophoresis [27]. For a neutral particle, an AC electric field can induce a dipole, which can then allow the particle to experience rotational or translational motion. Micro- and nanoparticles possess distinct biophysical characteristics that cause them to respond differently. Additionally, the electrical properties of the medium affect the response of the particles in the system. Lab-on-a-chip microdevices can utilize these AC electrokinetic effects to achieve controlled fluid flow and targeted manipulation of particles, such as cells. This can be useful for cell trapping, sorting, enrichment, and characterization.

“Nonuniform electric fields evoke unique and often puzzling effects on matter-even on matter that is electrically neutral” [9]. Dielectrophoresis (DEP), the electrokinetic phenomena used as a cell interrogation technique in this study, was thus described by Pohl [9]. Pohl published the first article on DEP in 1951 and followed up with further articles in the 1950s [28, 29], leading to early works by Pohl, Crane, and others further developing the theory and exploring applications of DEP, including separating living and dead yeast cells [30-32]. In 1978, Pohl authored a seminal book on the theory of DEP,

including comments on the effects of electrode geometry on DEP force, and the basis for manipulation of cells by DEP [9], topics especially pertinent to the work presented here.

An induced dipole forms on a neutral particle in the presence of a uniform electric field. However, barring the influence of another force, the particle will not move because the forces on the dipole are equal. In contrast, a non-uniform field will cause an imbalance of forces that results in particle motion. While original studies on DEP utilized pin-pin or pin-plate electrodes, advancements in microfabrication have enabled arrays of microelectrodes to be used for DEP [33]. Traveling wave dielectrophoresis (twDEP) arises from an electric field generated by planar electrodes for inducing horizontal particle motion of particles [34]. Numerical and analytical solutions to twDEP from interdigitated microelectrode arrays have been determined [35, 36]. In addition to translational particle motion, particles also demonstrate electrorotation which tends to align the dipole with the direction of the electric field. Dielectric properties of particles can be extracted by examining their electrorotation behavior [37, 38]. Dielectrophoretic effects can also occur on polarizable fluids, a phenomenon known as liquid dielectrophoresis [39], and can be used to create droplets or manipulate small volumes of fluid [40].

DEP has been used for a wide range of applications [41-45], including characterizing bioelectrical properties of cells and viruses [46-49], sorting cells based on viability [50] or distinct dielectric properties [51, 52], and screening for induced changes in biophysical properties of cells [53, 54]. Specifically, DEP has enabled drug screening [55], distinguishing between multidrug-resistant and sensitive cancer cells by their cytoplasmic conductivity [53, 56], and determination of cytoplasm and membrane conductivity of drug-treated red blood cells [37]. Further applications of DEP include cell viability determination [55, 57] and investigations of drug-stimulated cell surface roughness increase [58].

2.3 Development of Contactless Dielectrophoresis (cDEP)

Traditional DEP utilizes planar metallic electrodes patterned within a microfluidic channel to apply a voltage and induce a non-uniform electric field [9, 59]. While this is a powerful technique and has been successful for accomplishing the aforementioned applications, challenges can arise, such as electrode delamination and electrolysis at low-frequency operation. These challenges are a result of the contact between electrodes and the sample. Additionally, the electric field decreases exponentially from the electrode surface, limiting the size of the microchannels and thereby, the throughput.

Insulator-based dielectrophoresis (iDEP) [60] has addressed the challenges of fouling, electrode delamination, and spatial degradation of the electrode field through patterning insulating structures that induce non-uniformities in a DC electric field . The basic principle behind iDEP was published by Masuda *et al.* [61]. Lee *et al.* demonstrated insulator-based dielectrophoresis for a micromachined cell selector device [62]. iDEP was later achieved by arrays of insulating posts in a glass microchip [63] and used to sort live from dead cells [64] and concentrate microbes in water [65]. Polymeric iDEP devices with similar performance traits were developed to reduce cost and increase amenability to mass fabrication [66, 67]. iDEP operation typically involves inducing electrokinetic fluid flow via metal electrodes inserted in the inlet and outlet of the device, enabling throughput of biological sample without an external pressure-driven flow . Electric field gradients are induced via insulating structures, allowing trapping of targeted cells or molecules when the DEP force overcomes the EK flow. This method eliminates the need for expensive and complex microfabricated metal electrodes. iDEP has been used to selectively separate live and dead bacteria cells [60], isolate bacterial spores [67] and manipulate DNA [68], among other applications. However, Joule heating can be a challenge as a result of the high DC voltages required. To ameliorate this challenge, carbon-DEP [69] and contact-free DEP microdevices have been developed [70-72]. Carbon-DEP devices can be operated at lower voltages than iDEP, reducing the operational hazards while maintaining biocompatibility and reducing electrolysis compared to traditional DEP [33, 69].

One method to achieve contact-free operation involves mounting a PDMS microdevice on a 100 μm thin glass slide, and mounting the assembly on a reusable printed circuit board [71]. However, to fully remove the need for fabricating patterned metal electrodes, contactless dielectrophoresis (cDEP) was developed by substituting fluidic electrode channels separated by a thin 20 μm barrier from the sample channel [70]. By employing a highly conductive fluid in these side electrode channels, wire electrodes contacting fluid reservoirs can energize the fluid electrodes and thus enable an electric field. By applying an AC signal, the thin insulating barrier allows capacitive coupling of the fluid electrodes to the sample channel. The advantages of cDEP are manifold; electrode delamination, electrolysis, and Joule heating are avoided, while sterile conditions are supported, making cDEP ideal for handling biological samples, particularly when cell viability must be maintained. Practically, cDEP decreases costs and hazards associated with fabrication of metal patterned devices, since a single master can be used with polymer casting to make many inexpensive replicate devices. For scaling up to mass fabrication, the device can easily be produced by hot embossing or injection molding from a durable polymer such as polymethlymethacrylate (PMMA) or other biocompatible polymers.

Early cDEP devices were constrained to operation in high frequency ranges (100-500 kHz) [70, 73, 74]. Second generation devices were designed by Sano *et al.* for operation at low frequencies (<100 kHz) [75]. Low frequency operation is advantageous because mammalian cells show the greatest differences in crossover frequency, the point at which DEP force changes sign, at frequencies on the order of 1 kHz (see Theory section 5.2) [75]. By increasing the distance between fluid electrode channels to the order of centimeters, the resistance of the sample channel was increased, thus increasing the proportion of voltage drop occurring across the channel and lowering the operational frequency range. Additionally the capacitance of the barrier was increased by increasing the barrier area, contributing to the lower frequency operation. These devices effected continuous sorting of human leukemia monocytes from red blood cells, and have since been used for characterizing the crossover frequency and dielectric properties of murine ovarian cancer cells [76], and rare cells found in blood [77]. As an additional note, when operating these devices at frequencies near 1 kHz (ie. <10 kHz), some cells may appear

to die, likely due to AC electroporation effects [78]; experimentally, this effect is manifested in dyed cells that appear blurry, faint, and/or slightly enlarged (see Figure 13b. The fluorescent Calcein AM dye is enzymatically activated in the cytoplasm of the cell, and upon electroporation, enzymes and dye can leak out of the cell or cease to properly function, leading to the visual effects occasionally observed at very low frequencies.

A third iteration of devices theoretically applied the low frequency design to a multilayer device, in which fluidic electrode channels sandwich the sample channel from above and below, separated by thin insulating layers [79]. Experimental prototype devices achieved high throughput operation at 1 ml/hr while demonstrating that MDA-MB-231 breast cancer cells were trapped at 250 V_{rms} and 600 kHz in a prototype PMMA/PC (polycarbonate) device of somewhat different dimensions than the theoretical model. Low frequency continuous sorting should be demonstrable in devices that accurately reproduce the numerically-modeled geometry.

Multilayer devices can also be designed for high frequency operation. For example, a geometry wherein interdigitated electrodes channels overlap the sample channel while separated by a thin insulating barrier will lead to high frequency operation due to the close proximity of the source and sink electrode channels. The geometry of the electrodes determines the strength of the electric field gradient and the direction of cell translational motion. Curved interdigitated electrodes of narrowing width change the angle and magnitude of the DEP force across the width of the channel, potentially allowing sorting of more than two cell types in a “rainbow” method.

2.4 DEP & cDEP for Cell Sorting and Characterization

Biological analyses such as immunofluorescence microscopy, fluorescence-activated cell sorting (FACS), immunocytochemistry, cell-based enzyme-linked immunosorbent assay (ELISA), DNA staining, Western blots, and others, require sufficient amount of cell sample to provide enough sample to reach detection limits. As a result, enrichment techniques are necessary to concentrate the sample amount relative to the background. Cell enrichment techniques include physical filtration, density-based gradient separation,

and immunomagnetic cell separation (also known as magnetic-activated cell sorting, MACS) [80]. Other cell sorting and enrichment strategies include hydrodynamic [81] or inertial [82, 83] sorting, and non-inertial methods [84] such as optical tweezers [85, 86], acoustophoresis [87], dielectrophoresis [88, 89], and combinations thereof [51, 90, 91]. However, these techniques either rely on known surface markers or significant size/density-based differences between cell types.

The most commonly used sensitive enrichment techniques are FACS [92] and MACS [93-95], which rely upon expressed surface markers to differentiate cells. FACS operates by hydrodynamically focusing a stream of cells which are then excited to fluoresce, and sorted by selectively applying a surface charge to each droplet. Because each cell is sorted individually, high purity can be achieved. However, the serial sorting limits throughput to the scale of 1E5 particles/second [96]. The advantage of MACS, which tags cells and magnetically deflects their flow trajectories, consists of higher throughput because targeted cells can be sorted in parallel. However, there is a wide range of sorting purity and recovery [95]. DEP-based methods eliminate the need for labeling of target cell populations based on previously-determined expression levels of biomarkers, and rather interrogate cells based on their intrinsic biophysical properties.

Since the early use of DEP to separate living and dead yeast cells [30], DEP has been utilized for cell enrichment [97], isolation , characterization [46, 47, 98], sorting [90], and single-cell manipulation [99-101]. Several helpful reviews of the status of DEP have been published in the last few years, including a comprehensive review by Pethig [44], a review of cell-focused DEP by Gagnon [102], and a review of DEP for diagnostics by Gascoyne [103].

Studies using cDEP have focused on bulk cell sorting and characterization rather than single-cell analysis. cDEP has successfully differentiated between living and dead leukemia cells [73], selectively isolated breast cancer cells based on stage [74], characterized dielectric properties of red blood cells, macrophages, leukemia cells, and breast cancer cells [104], isolated cancer cells from dilute whole blood [75], and tumor

initiating cell from prostate cancer cells [105], showed that late stage ovarian cancer cells presented different dielectric responses from peritoneal cells [106], and distinguished amongst stages of a syngeneic mouse cell model for progressive ovarian cancer [76].

The quantified dielectric properties of different stages of this progressive cancer model laid the immediate foundation for the study presented in this thesis. In this mouse model, isolated primary mouse ovarian surface epithelial (MOSE) cells undergo transformation in vitro and progress to malignant stages [107]. Since human cell lines providing different stages of ovarian cancer derived from one genetic source are not available for study, the MOSE model represents a useful alternative that avoids the potential confounding variable of inter-subject genetic differences. An increasingly dysregulated cytoskeleton organization and changes in the expression of cytoskeleton genes and their regulators were observed during neoplastic progression, accompanied by an increase in membrane ruffles and protrusions [107, 108]. Cytoskeletal changes were associated with stage-specific changes in cellular biomechanical properties [109]. The membrane capacitance was greater in malignant cells than in early-stage cells [76].

DEP has been successfully used for drug screening applications [55], to distinguish between multidrug-resistant and sensitive cancer cells by their cytoplasmic conductivity [53, 56], and to determine cytoplasm and membrane conductivity of drug-treated red blood cells [37]. Further applications of DEP include cell viability determination [55], [57] and investigations of drug-stimulated cell surface roughness increase [58]. These applications are possible due to the physiological changes induced by drugs which correlate to changes in electrical signature.

Chapter 3 Dielectrophoretic Theory

To predict the motion of a cell in a microfluidic cDEP device, the external forces acting on the cell must be determined, and the biophysical characteristics of the cell itself must be considered. At the microscale, the ratio of surface area to volume is much increased compared to the macroscale, causing surface forces such as frictional forces, capillary forces, electrostatic forces and surface tension to become the prominent influences on particle and fluid behavior, rather than inertial forces such as gravity. Here we focus on the targeted application of forces arising from an external non-uniform electric field to direct translational motion of particles suspended in a laminar liquid flow. Because cells are suspended in a pressure-driven liquid the force arising from the microfluidic flow is a major actor on the cells. The other main impetus for cell motion is the dielectrophoretic force which arises from an applied non-uniform electric field. In this chapter dielectrophoretic behavior of the cell is first derived from the assumption of the cell as a spherical particle, and then expanded to account for the complex structure of the cell.

3.1 Fluid Flow in Microchannels

The behavior of fluids at the microscale is greatly influenced by the large surface area to volume ratio compared to the macroscale. The dimensionless Knudsen number, Kn, is helpful to discern the physical regime of the problem at hand,

$$Kn = \frac{\lambda_f}{L} \tag{3.1.}$$

where λ_f is the mean free path and L is the characteristic length scale. For pressure-driven flow of gases, continuum mechanics may be used where $Kn \ll 1$, the fluid can be described as having slip boundary conditions where $Kn \sim 1$, and continuum mechanics break down for $Kn \gg 1$ [110]. For liquids, due to greater incompressibility, the continuum approach breaks down at the molecular scale, though some uncertainty exists about the nature and theory of apparent slip at the boundaries [110].

The velocity of the fluid is described by the Navier-Stokes equation,

$$\rho\left(\frac{\partial \mathbf{u}}{\partial t} + \mathbf{u} \cdot \nabla \mathbf{u}\right) = \nabla \cdot \overleftrightarrow{\boldsymbol{\sigma}} + \mathbf{f} = -\nabla p + \eta \nabla^2 \mathbf{u} + \mathbf{f} \tag{3.2.}$$

where ρ is the fluid density, $\mathbf{u}$ is the fluid velocity, t is the time, $\vec{\vec{\sigma}}$ is the tensor stress, $\mathbf{f}$ represents the body force densities, p is the pressure, and η is the viscosity [110].

Microfluidic flow occurs in the laminar flow regime, which is quantified by the Reynolds number, Re,

$$\mathrm{Re} \equiv \frac{\rho U_0 L_0}{\eta} \tag{3.3.}$$

where U_0 is the fluid velocity and L_0 is the characteristic length. The laminar flow regime in a circular pipe exists at about Re<2500. However, in microfluidic flow situations, viscous forces dominate inertial forces to the extent that typical values of Reynolds numbers are <1, and inertial effects are generally negligible. Neglecting inertial effects in the Navier-Stokes Equation (3.2) leads to neglecting the acceleration term on the left-hand side.

3.2 Stokes Drag

The forces on a single particle in a microfluidic channel include the drag force from pressure-driven flow. Stokes drag regime occurs at low particle Reynolds numbers. The Reynolds number for a single particle is

$$Re_P = DU\rho_f/\eta_f \tag{3.4.}$$

Where D is the particle diameter, U is the velocity of the fluid, ρ_f is the density of the fluid, and η is the viscosity of the fluid. The coefficient of drag for particle numbers less than 1.0 is

$$C_D = 24/Re_p \tag{3.5.}$$

At very low Reynolds numbers, the Stokes drag force on a spherical particle is described as,

$$\boldsymbol{F_{drag}} = 6\eta\pi(\boldsymbol{u_p} - \boldsymbol{u_f}) \tag{3.6.}$$

where $\boldsymbol{u_p}$ and $\boldsymbol{u_f}$ are the velocities of the particle and suspending fluid, respectively. To achieve targeted deflection or trapping of particles and cells by cDEP, the Stokes drag force must be overcome by the dielectrophoretic force. Specifically, when considering unidirectional flow in a straight channel, the drag force acts in the positive x-direction, so the dielectrophoretic force must act at an angle that results in deflect cells of interest from

their previous streamlines to new streamlines leading to specified collection reservoirs. We now turn our attention to the development of this dielectrophoretic force.

3.3 Force on a Dipole

Figure 1 shows an induced dipole of two opposite charges, $+q$ and $-q$, on a neutral particle located in an electric field. The dipole moment vector, $\boldsymbol{p}$, depends on the charge, q, and position vector, $\boldsymbol{d}$, between the poles:

$$\boldsymbol{p} = q\boldsymbol{d} \tag{3.7.}$$

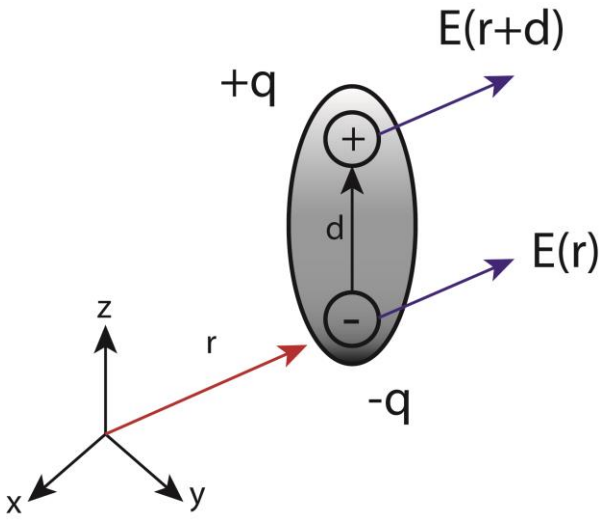

Figure 1. A dipole is induced on a particle in an external electric field, E. The poles are separated by the distance d, and have positive charge +q, and negative charge –q. The electric field acting on each charge is represented by E(r) and E(r+d).

There is a net force acting on the dipole, as the additive result of the vector forces at each pole (adapted from Jones [111] and dissertation [112])

$$\boldsymbol{F} = q\boldsymbol{E}(\boldsymbol{r} + \boldsymbol{d}) - q\boldsymbol{E}(\boldsymbol{r}) \tag{3.8.}$$

The distance between the poles, $\boldsymbol{d}$, can be assumed infinitesimal by comparing the dimensions of the particle to the dimensions of the electrodes; specifically, the particle is much smaller than the scale of the electric field gradients.

In general, the Taylor series expansion is described by

$$f(x) \approx \frac{f(a)}{0!} + \frac{f'(a)}{1!}(x-a) + \frac{f''(a)}{2!}(x-a)^2 + \frac{f'''(a)}{3!}(x-a)^3 + \cdots + \frac{f^n(a)}{n!}(x-a)^n + \cdots \quad \textbf{(3.9.)}$$

The Taylor series expansion for $\boldsymbol{E}(\boldsymbol{r}+\boldsymbol{d})$ is

$$\boldsymbol{E}(\boldsymbol{r}+\boldsymbol{d}) = \sum_{j=0}^{\infty}\left[\frac{1}{j!}(\boldsymbol{d}\cdot\boldsymbol{\nabla})^{\mathrm{j}}\,\boldsymbol{E}(\boldsymbol{r})\right] \quad \textbf{(3.10.)}$$

where the series is traditionally approximated by the first two terms due to the assumption of infinitesimal $\boldsymbol{d}$ **[111]**:

$$\boldsymbol{E}(\boldsymbol{r}+\boldsymbol{d}) \cong \boldsymbol{E}(\boldsymbol{r}) + (\boldsymbol{d}\cdot\boldsymbol{\nabla})\boldsymbol{E}(\boldsymbol{r}) \quad \textbf{(3.11.)}$$

By substituting the traditional approximation using the first two terms into Eqn 3.6, and using the definition of the dipole moment (Eqn 3.5), we find the net force on an infinitesimal dipole:

$$\boldsymbol{F}_{\boldsymbol{dipole}} = [q\boldsymbol{E}(\boldsymbol{r}) + \boldsymbol{q}(\boldsymbol{d}\cdot\boldsymbol{\nabla})\boldsymbol{E}(\boldsymbol{r})] - q\boldsymbol{E}(\boldsymbol{r}) \quad \textbf{(3.12.)}$$

$$\boldsymbol{F}_{\boldsymbol{dipole}} = \boldsymbol{q}(\boldsymbol{d}\cdot\boldsymbol{\nabla})\boldsymbol{E}(\boldsymbol{r}) \quad \textbf{(3.13.)}$$

$$\boldsymbol{F}_{\boldsymbol{dipole}} = (\boldsymbol{p}\cdot\boldsymbol{\nabla})\boldsymbol{E}(\boldsymbol{r}) \quad \textbf{(3.14.)}$$

For this dipole in a medium with dielectric constant $\boldsymbol{\epsilon_i}$, the electrostatic potential in spherical coordinates is [113]

$$\phi_{dipole} = \frac{p\cos\theta}{4\pi\epsilon_i r^2} \quad \textbf{(3.15.)}$$

3.4 Effective Dipole Moment of a Lossless Dielectric Spherical Particle

To determine the effective induced dipole moment of a spherical particle, the particle may be modelled as a homogeneous sphere, single-shell particle, or multi-shell particle [114]. Shell models are useful for biological particles with complex interior structures. Using Eqn 3.12, the potential on an induced dipole, with the potential of a single-shell model of a spherical particle, we can determine the induced dipole moment for a lossless spherical dielectric particle in an external electric field. Making the assumption of a lossless particle indicates that the induced dipole does not lag the electric field.

For a net-neutral particle of radius R in an external uniform electric field, the Laplace boundary conditions must be satisfied. There must be continuity of the electric potential, ϕ, and the radial displacement flux, $\frac{\partial \phi}{\partial r}$, at the interface between the medium and outer membrane of the particle ($R = R_2$), and at the interface between the inner shell, representing cytoplasm, and the membrane ($R = R_3$).

Additionally, the solution of the Laplace equation outside and inside of the particle can be described as follows:

outside: $$\phi_1(r,\theta) = -Ercos\theta + \frac{Acos\theta}{r^2}, \qquad \text{at } r > R_2 = R \tag{3.16.}$$

shell: $$\phi_2(r,\theta) = -Brcos\theta + \frac{Ccos\theta}{r^2} \quad \text{at } R_2 > r > R_3 \tag{3.17.}$$

inside: $$\phi_3(r,\theta) = -Drcos\theta, \qquad \text{at } r < R_3 \tag{3.18.}$$

Therefore the constants can be determined as:

$$A = \frac{\epsilon_2 - \epsilon_1}{\epsilon_2 + 2\epsilon_1} R^3 E \tag{3.19.}$$

$$B = \frac{3\epsilon_1}{\epsilon_2 + 2\epsilon_1} E \qquad \textbf{(3.20.)}$$

By comparing the electrostatic potential for a dipole with the determined equations above for a single-shell sphere, the effective dipole moment, where ϵ^*_{eff} is the effective complex permittivity accounting for the shell and interior, is:

$$p_{eff} = 4\pi\epsilon_1 r^3 \frac{\left(\epsilon^*_{eff} - \epsilon^*_i\right)}{\epsilon^*_{eff} + 2\epsilon^*_i} E \qquad \textbf{(3.21.)}$$

From this, the time averaged DEP force can be determined by substituting the expression for the induced dipole moment of the single-shell sphere into the force expression for an infinitesimal dipole:

$$\boldsymbol{F_{DEP}} = p_{eff} \cdot \nabla E = 2\pi a^3 \epsilon_i \frac{\left(\epsilon^*_{eff} - \epsilon^*_i\right)}{\epsilon^*_{eff} + 2\epsilon^*_i} \nabla(\boldsymbol{E} \cdot \boldsymbol{E}) \qquad \textbf{(3.22.)}$$

A dielectric material possessing surface charge attracts opposite charges and repels like charges of an ionic medium when an external electric field is applied. The result of the electrical and diffusion forces is a double layer of charge. The layer of fixed charges is known as the Stern layer, while the layer of mobile charges is known as the Debye layer. The overall phenomenon is known as the electric double layer (EDL), and when occurring in a fluid along a microchannel wall, can support the rise of electro-osmotic flow. The electrostatic force decays away from the wall, allowing the ions in the bulk fluid to move parallel to the channel wall. In contrast, when this action occurs at the interface between a charged particle and an infinite ionic fluid, the particle will move toward the area with highest potential, a motion known as electrophoresis. In the special case of a neutral polarizable particle in a uniform external field, no force will arise due to the net neutral charge. However, when an EDL develops for a net neutral but polarizable particle in a nonuniform electric field, a phenomenon known as dielectrophoresis occurs.

3.5 Cells and Particles in Non-uniform Electric Fields

A neutral particle submerged in an electrolyte fluid under an electric field may exhibit a dipole. Surface charges align themselves in relation to an externally applied electric field and an imbalance of charges can result, with one region on the particle being positively charged and one region negatively charged, but both charges of equal magnitude. Free charges from the solution align themselves to the charged regions on the surface of the particle in response. The ability of the charges to distribute around a particle in response to an external electric field is termed polarizability.

Bound charges align at the surface forming what is known as the Stern layer, while free charges of opposite charge are attracted and align as a second layer, forming an interfacial double layer [115]. At high AC frequencies, the free charge cannot switch polarization quickly enough to keep pace with the current, at which point the permittivity of the particle becomes dominant. A relaxation frequency exists at each dispersion due to interfacial polarization [116]. For a cell, which has an outer bilayer membrane and a nuclear membrane, two relaxation frequencies exist, so two crossover frequencies exist. In comparison, a solid particle has one crossover frequency due to possessing only a single interface [115]. The curve of the CM factor changing with frequency is altered based on changes in the cell traits, such as size, membrane topography, and nuclear-cytoplasm ratio [47]. For a thorough review of DEP and other AC electrokinetic phenomena, see the book authored by Morgan and Green [115].

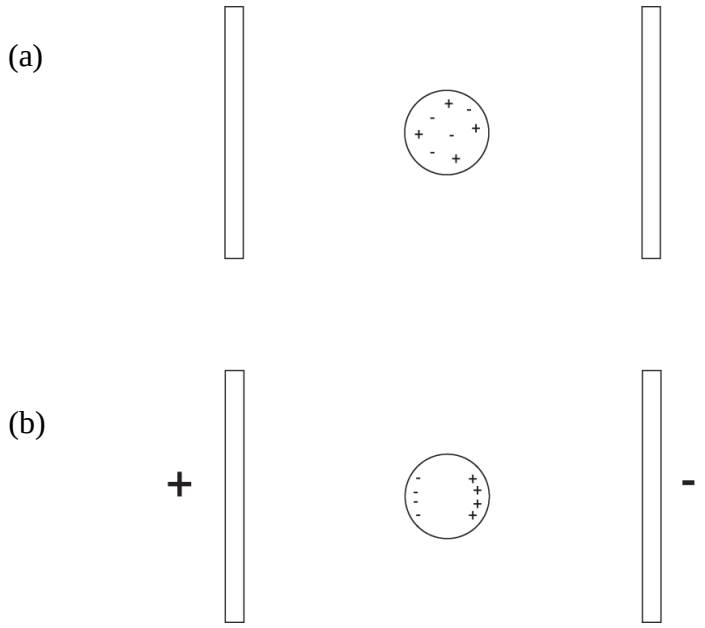

Figure 2. . (a) A neutral particle is not polarized without an external electric field. (b) A neutral particle polarizes under an external electric field, resulting in an induced dipole.

In the case of a charged particle in a uniform external electric field, such as that generated by a DC signal, a translational electrophoretic force will act to attract or repel the charged particle towards or away from the positive and negative poles of the electric field, depending on the sign of the particle's charge. However, a uniform external electric field can induce a dipole on a neutral particle (as previously discussed), but will not cause a translational force due to the net neutrality of the particle. A rotational force, or torque, **Γ,** will be experienced by the particle and tends to align the dipole with the field:

$$\boldsymbol{\Gamma} = \boldsymbol{p} \times \boldsymbol{E} \qquad \textbf{(3.23.)}$$

In contrast, a non-uniform electric field will cause a translational force on an induced dipole because of the non-zero gradients of the electric field. The force causing translational movement of a polarized particle in a non-uniform electric field is called dielectrophoresis (DEP).

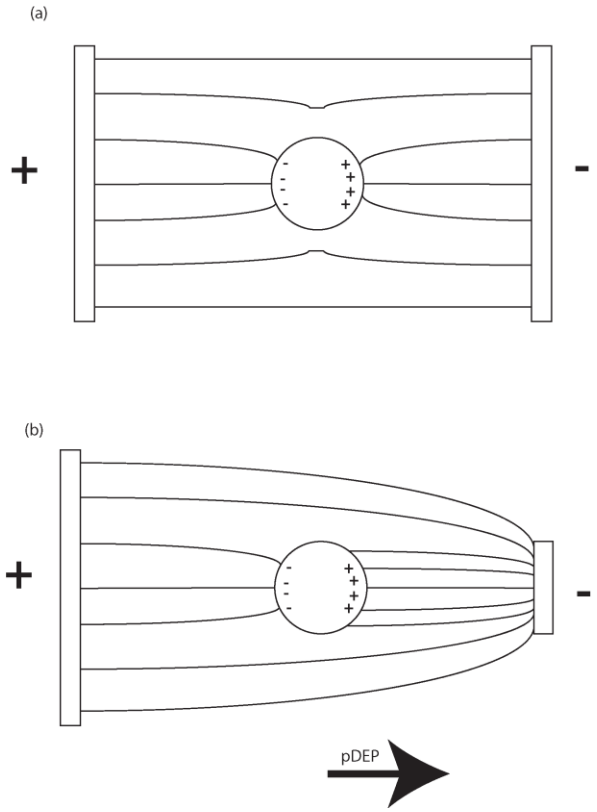

Figure 3. . (a) A polarized particle in a uniform electric field does not experience a net force. (b)A polarized particle in a non-uniform field experiences a net force, as illustrated by the positive dielectrophoretic force directing the particle to the region of high electric field gradients.

The dielectrophoretic (DEP) force, $\boldsymbol{F_{DEP}}$, on a solid lossy spherical particle, such as a latex (polystyrene) microsphere, is described as

$$\boldsymbol{F_{DEP}} = 2\pi a^3 \epsilon_m Re[K(\omega)]\nabla(\boldsymbol{E}\cdot\boldsymbol{E}) \quad \textbf{(3.24.)}$$

where a is the radius of the particle, ϵ_m is the permittivity of the suspending medium, and $Re[K(\omega)]$ represents the real part of the frequency-dependent Clausius-Mossotti (CM) factor [9]. The DEP force scales with the radius cubed, indicating the strong influence that particle size has in determining the DEP force experienced by the particle. The CM factor relates the relative polarizability of a particle to the suspending medium, and for a solid sphere is represented by

$$K(\epsilon_p^*, \epsilon_m^*) = \frac{\epsilon_p^* - \epsilon_m^*}{\epsilon_p^* + 2\epsilon_m^*} \quad \textbf{(3.25.)}$$

where $\epsilon_p^*, \epsilon_m^*$ are the complex permittivities of the particle and the suspending medium, respectively. Permittivity is the constant of proportionality between the electric field and

the electric susceptibility, a measure of how easily a dipole polarizes in an electric field. Therefore, permittivity describes how much electric flux is generated in response to charge moving through a particle. The complex permittivity is frequency-dependent and described as

$$\epsilon^* = \epsilon + \frac{\sigma}{j \cdot \omega} \quad \textbf{(3.26.)}$$

where $j = \sqrt{-1}$, ω is the angular frequency, and σ is the conductivity. For a lossy particle in a suspending medium, the amount of surface charge at the particle-medium interface is frequency dependent and the system exhibits dispersion. There is a Maxwell-Wagner relaxation time, τ_{MW}, for the effective permittivity,

$$\tau_{MW} = \frac{\epsilon_p - \epsilon_m}{\sigma_p + 2\sigma_m} \quad \textbf{(3.27.)}$$

where ϵ_p is the relative permittivity of the particle and σ_p, σ_m are the conductivity values of the particle and medium, respectively [111, 115]. The characteristic time is associated with the relaxation frequency, the frequency at which the maximum polarization occurs [114]. For a dielectric particle, a lag exists between the harmonically oscillating AC signal and the frequency-dependent polarization of the particle. As the frequency increases, the particle has less time to relax and respond to the field, eventually leading to a relaxation frequency at which the maximum energy is dissipated by the system [114]. Above this frequency, maximum polarization does not occur. When the amount of time for the dipole to align with the electric field and the time required for the field to change directions are equivalent, that period is called the Maxwell-Wagner relaxation time.

When the particle is a cell, the models must be adapted to account for a much more complex structure [116]. Bound by a phospholipid bilayer membrane, cells contain a myriad of organelles as well as the nucleus, all of which are surrounded by cytoplasm. These physical characteristics influence dielectric properties of the cell. A nonhomogeneous particle, such as a cell, can be modeled as a series of concentric spherical shells.

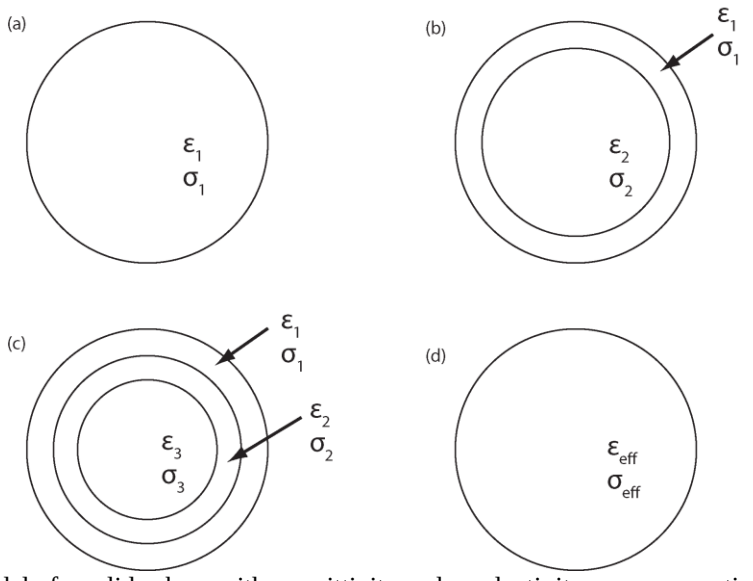

Figure 4. (a) A model of a solid sphere with permittivity and conductivity ϵ_1, σ_1 respectively, represents a particle such as latex bead. (b) A single-shell model of a cell with different permittivities and conductivities for the outer shell 1, and a homogeneous inner shell 2 represent the cell membrane and a homogeneous interior. (c) A multi-shell model with distinct permittivities and conductivities can represent a cell with an outer membrane, 1, interior structures, 2, and nuclear membrane, 3. (d) Effective values of the permittivity and conductivity are calculated from the values for each shell, simulating a smeared-out value for the spherical particle.

The simplest model accounts for the cell membrane as an outer shell and the cell cytoplasm as an interior sphere, where the dielectric properties of each region are given effective values. For example, the single-shell model requires an effective permittivity of

$$\epsilon_{23}^* = \epsilon_2^* \left[\gamma_{12}^3 + 2\left(\frac{\epsilon_3^* - \epsilon_2^*}{\epsilon_3^* + 2\epsilon_2^*}\right)\right] / \left[\gamma_{12}^3 - \left(\frac{\epsilon_3^* - \epsilon_2^*}{\epsilon_3^* + 2\epsilon_2^*}\right)\right] \quad \textbf{(3.28.)}$$

where $\gamma_{12} = a_1/a_2$ [108][102][97]. A more detailed multi-shell model consists of an outer shell representing the membrane, a second inner shell representing the cytoplasm, and an interior sphere representing the cell nucleus. In this case, ϵ_3^* from Equation (3.24) is replaced by the following expression accounting for interface between the cytoplasm and nuclear membrane:

$$\epsilon_{34}^* = \epsilon_3^* \left[\gamma_{23}^3 + 2\left(\frac{\epsilon_4^* - \epsilon_3^*}{\epsilon_4^* + 2\epsilon_3^*}\right)\right] / \left[\gamma_{23}^3 - \left(\frac{\epsilon_4^* - \epsilon_3^*}{\epsilon_4^* + 2\epsilon_3^*}\right)\right] \quad \textbf{(3.29.)}$$

where $\gamma_{23} = a_2/a_3$ [115]. This procedure can be continued for each additional shell as well.

The CM factor is theoretically bound between -0.5 and 1. As evidenced by Equation (3.20). the sign of the CM factor dictates the direction of the dielectrophoretic force. The frequency at which the real part of the CM factor equals zero is termed the crossover frequency, and is the frequency at which the particle experiences no dielectrophoretic force. When the CM factor is positive, the particle is more polarizable than the suspending medium and moves toward areas of high electric field strength. When the CM factor is negative, the particle is less polarizable than the suspending medium and is repelled from regions of high electric field strength.

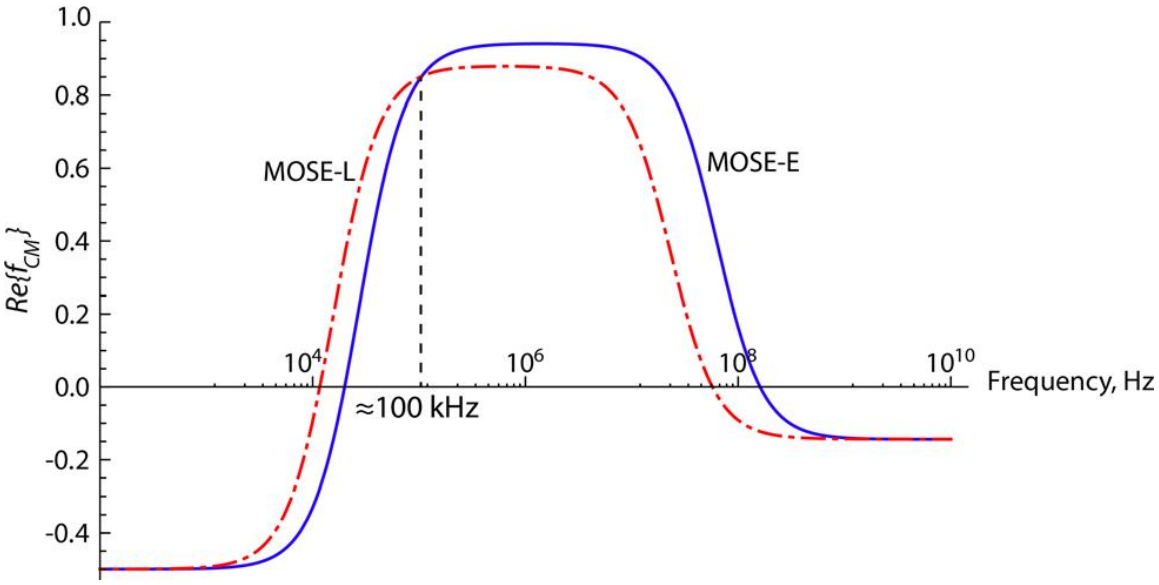

Figure 5. The plot by Salmanzadeh *et al.* [76] exemplifies the theoretical behavior of the real part of the CM factor over a frequency range, indicating two crossover frequencies due to interfacial polarization in the cell.

The crossover frequency, the frequency at which the real part of the Clausius-Mossotti factor, $Re[K(\omega)]$, equals zero, is derived as follows:

$$K(\epsilon_p^*, \epsilon_m^*) = \frac{\epsilon_p^* - \epsilon_m^*}{\epsilon_p^* + 2\epsilon_m^*} \quad \textbf{(3.30.)}$$

$$K(\epsilon_p^*, \epsilon_m^*) = \frac{[\epsilon_p + \sigma_p/(j\omega)] - [\epsilon_m + \sigma_m/(j\omega)]}{[\epsilon_p + \sigma_p/(j\omega)] + 2[\epsilon_m + \sigma_m/(j\omega)]} \quad \textbf{(3.31.)}$$

$$K\left(\epsilon_p^*, \epsilon_m^*, \omega\right) = \frac{\left[\epsilon_p - \epsilon_m + \frac{\sigma_p}{j\omega} - \frac{\sigma_m}{j\omega}\right]}{\left[\epsilon_p + 2\epsilon_m + \frac{\sigma_p}{j\omega} + \frac{2\sigma_m}{j\omega}\right]} = \frac{\epsilon_p - \epsilon_m + \frac{\sigma_p - \sigma_m}{j\omega}}{\epsilon_p + 2\epsilon_m + \frac{\sigma_p + 2\sigma_m}{j\omega}}$$

$$= \frac{(\epsilon_p - \epsilon_m) + \frac{\sigma_p - \sigma_m}{j\omega}}{(\epsilon_p + 2\epsilon_m) + \frac{\sigma_p + 2\sigma_m}{j\omega}} * \frac{(\epsilon_p + 2\epsilon_m) - \frac{\sigma_p + 2\sigma_m}{j\omega}}{(\epsilon_p + 2\epsilon_m) - \frac{\sigma_p + 2\sigma_m}{j\omega}} \quad \textbf{(3.32.)}$$

$$= \frac{(\epsilon_P - \epsilon_m)(\epsilon_p + 2\epsilon_m) + \left(\frac{\sigma_p - \sigma_m}{\omega}\right)\left(\frac{\sigma_p + 2\sigma_m}{\omega}\right)}{\left(\frac{\sigma_p - \sigma_m}{\omega}\right)^2 + \left(\frac{\sigma_p + 2\sigma_m}{\omega}\right)^2} + j\frac{(\epsilon_p + 2\epsilon_m)\left(\frac{\sigma_p + 2\sigma_m}{\omega}\right) - \left(\frac{\sigma_p - \sigma_m}{\omega}\right)(\epsilon_p - \epsilon_m)}{\left(\frac{\sigma_p - \sigma_m}{\omega}\right)^2 + \left(\frac{\sigma_p + 2\sigma_m}{\omega}\right)^2}$$

$$Re\left[K\left(\epsilon_p^*, \epsilon_m^*, \omega\right)\right] = \frac{(\epsilon_P - \epsilon_m)(\epsilon_p + 2\epsilon_m) + \left(\frac{\sigma_p - \sigma_m}{\omega}\right)\left(\frac{\sigma_p + 2\sigma_m}{\omega}\right)}{\left(\frac{\sigma_p - \sigma_m}{\omega}\right)^2 + \left(\frac{\sigma_p + 2\sigma_m}{\omega}\right)^2} \quad \textbf{(3.33.)}$$

$$Re[K(\omega)] = 0 = (\epsilon_P - \epsilon_m)(\epsilon_p + 2\epsilon_m) + \left(\frac{\sigma_p - \sigma_m}{\omega}\right)\left(\frac{\sigma_p + 2\sigma_m}{\omega}\right) \quad \textbf{(3.34.)}$$

$$-(\epsilon_P - \epsilon_m)(\epsilon_p + 2\epsilon_m) = \left(\frac{\sigma_p - \sigma_m}{\omega}\right)\left(\frac{\sigma_p + 2\sigma_m}{\omega}\right)$$

$$-\omega^2 = \frac{(\sigma_p - \sigma_m)(\sigma_p + 2\sigma_m)}{(\epsilon_p - \epsilon_m)(\epsilon_p + 2\epsilon_m)} \quad \textbf{(3.35.)}$$

$$\omega_{xo} = \sqrt{\frac{-(\sigma_p + 2\sigma_m)(\sigma_p - \sigma_m)}{(2\epsilon_m + \epsilon_p)(\epsilon_p - \epsilon_m)}} \quad \textbf{(3.36.)}$$

$$f_{xo} = \frac{1}{2\pi}\sqrt{\frac{-(\sigma_p - \sigma_m)(\sigma_p + 2\sigma_m)}{(\varepsilon_p - \varepsilon_m)(\varepsilon_p + 2\varepsilon_m)}} \quad \textbf{(3.37.)}$$

By setting this expression for the real part of the Clausius-Mossotti factor to equal zero, the crossover frequency can be calculated (Eqn. 3.37). The crossover frequency has a linear relationship with conductivity:

$$f_{xo} = \frac{\left(\sqrt{2}\,\sigma_m\right)}{2\pi r C_{mem}} \quad \textbf{(3.38.)}$$

An alternative form of the real part of the Clausius-Mossotti factor emphasizes the role of frequency and the Maxwell-Wagner relaxation time [111].

$$Re[K(\omega)] = \frac{\epsilon_2 - \epsilon_1}{\epsilon_2 + 2\epsilon_1} + \frac{3(\epsilon_1\sigma_2 - \epsilon_2\sigma_1)}{\tau_{MW}(\sigma_2 + 2\sigma_1)^2(1 + \omega^2\tau_{MW}^2)} \quad \textbf{(3.39.)}$$

Taking only the imaginary part of the Clausius-Mossotti factor yields [99]

$$Im[K(\omega)] = \frac{3\omega\tau_{MW}(\epsilon_p\sigma_m - \epsilon_m\sigma_p)}{(1 + \omega^2\tau_{MW}^2)(\epsilon_p + 2\epsilon_m)(\sigma_p + 2\sigma_m)} \quad \textbf{(3.40.)}$$

Upon extracting the crossover frequency, the specific membrane capacitance of cells can be calculated. Mammalian cancer cells have first crossover frequencies under 100 kHz, so devices to characterize these cells would ideally operate in this "low" frequency range. However, due to the influence of traits such as the nucleus to cytoplasm ratio, which influence the second crossover frequency, cells may still be selectively sorted or deflected at frequencies higher than the first crossover frequency. The application portion of this work relies upon low frequency interrogation of cell crossover frequencies, while the device design portion takes advantage of differences in cell populations at higher frequencies.

Chapter 4. Methods

4.1 SU-8 Master Fabrication

To make multilayer cDEP devices having a sample channel layer and an electrode channel layer, two separate masters were fabricated from silicon wafers. Because the resolution of the features was above 20μm, a relatively simple microfabrication technique was used; rather than etching the silicon wafer itself, SU-8 photoresist was deposited on the wafer and then etched in the pattern of the channels. One master was etched with the electrode channel pattern, and the other master was etched with the sample channel pattern.

A silicon wafer was placed in Cyantek Nano-Strip (Cyantek, Fremont, CA, USA) for 10 minutes at room temperature. The wafer was rinsed with deionized (DI) water and placed in buffered ion etch (BOE), hydrofluoric acid buffered with ammonia, for 2 minutes. The wafer was rinsed with DI water. The wafer was spun at 3000 rpm while rinsing consecutively with acetone, isopropyl alcohol (IPA), and DI water, and allowed to spin for 30 seconds to dry. The wafer was placed on a hot plate at 110˚C for 1 minute. A small amount of MCC Primer 80/20 adhesion promoter (MicroChem Corp., Newton, MA, USA) was deposited on the wafer and spun at 3500 rpm for 30 seconds then placed on the hot plate at 115˚C for 3 minutes. Four milliliters for a 4-inch silicon wafer of SU-8 2000 permanent epoxy negative photoresist (MicroChem Corp., Newton, MA, USA) was required. The photoresist was spun according to the manufacturer instructions to achieve the desired thickness. For this case, 50 μm thickness was achieved by spinning at 500 rpm for 7 seconds, 900 rpm for 5 seconds, and 1750 rpm for 27 seconds. The photoresist was underwent a soft bake according to manufacturer instructions: 1 minute at 65 ˚C, ramp the temperature to 95 ˚C for 7 minutes. The hot plate was turned off and the wafer was allowed to cool down on the hot plate to room temperature, for approximately 20 minutes. The wafer was placed in SU-8 developer (MicroChem Corp., Newton, MA, USA) for 4 minutes, gently agitating at 30 second intervals. The wafer was removed and rinsed with IPA.

4.2 Low Frequency Device Fabrication

The silicon master for low frequency devices was fabricated using deep reactive ion etching (DRIE) because of its suitability for small feature sizes, such as the 20 μm barrier between the sample and electrode channels. The master was fabricated prior to this work, as described in [77], and fresh microdevices were fabricated from the master for the experiments described here.

cDEP devices were fabricated from polydimethylsiloxane (PDMS). PDMS was mixed in a 10:1 ratio of elastomer to curing agent (Sylgard 184, Dow Corning, USA). The liquid-phase PDMS was left under vacuum for 30 minutes degas. Aluminum foil was carefully folded around the wafer to form short walls around the edge of the wafer, preventing liquid PDMS from overflowing the stamp edges. The liquid PDMS was then poured onto the silicon master stamp, and cured for 45 minutes at 100°C. After allowing the device and wafer to cool for 5-10 minutes, the aluminum foil and device were peeled off the wafer. Excess PDMS was trimmed and fluidic connections were punched in the inlet and outlet of each channel with a 1.5 mm core sample cutter (Harris Uni-Core, Ted Pella, Inc., Redding, CA).

The devices were cleaned using clear 3M Scotch Magic tape (3M, St. Paul, MN, USA) and examined under the microscope to ensure removal of particulates from the channels. A 2”x3” 1.0 mm thick glass microscope slide (Premiere, China) was cleaned with soap and tap water, then ethanol, followed by a DI water rinse and drying using pressurized air. The cleaned microdevice and glass slide were placed in an air plasma cleaner (Harrick Plasma, Ithaca, NY, USA). The pump was turned on for two minutes, at which time the plasma was powered on and the RF level was turned to “Hi”. The device and slide were exposed to plasma for two minutes after visually ascertaining the appearance of a bright fuschia color interior to the plasma cleaner. After powering down, the device was quickly bonded to the glass slide by manually pressing from the center to the outside edges of the device, ensuring no air bubbles or collapsed channels were formed.

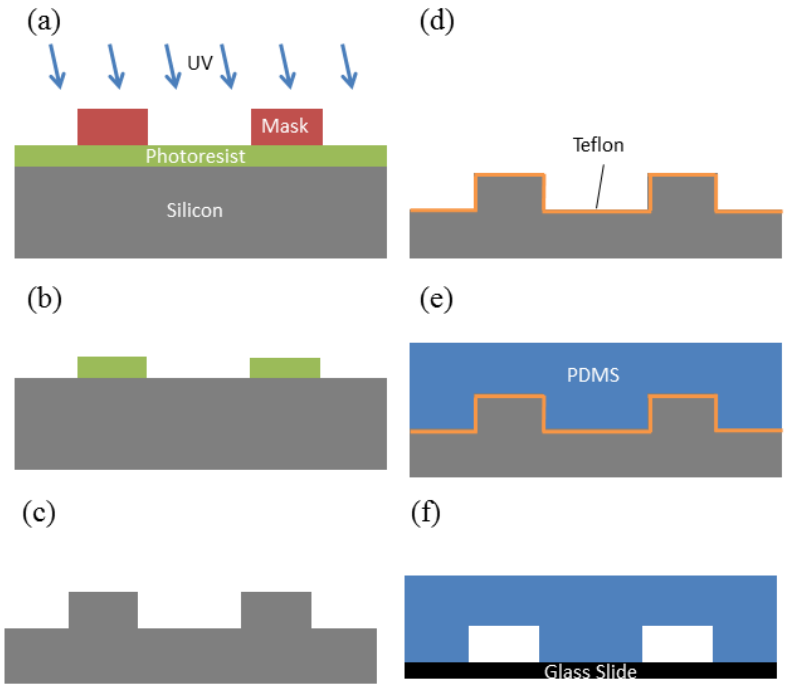

Figure 6. Fabricating a silicon wafer master and PDMS microfluidic device. (a) Photoresist is patterned in the device geometry by exposure to UV light through a transparency mask. (b) Exposed photoresist is removed by washing with developer. (c) The exposed silicon is etched using deep reactive ion etching (DRIE). (d) Remaining photoresist is removed and a thin Teflon coating is applied to facilitate release of PDMS from the master. (e) Liquid PDMS is poured onto the silicon wafer and cured. (f) Solid PDMS is bonded to a glass slide to close the microchannels.

4.3 Multilayer Device Fabrication

The multilayer cDEP devices consisted of a slab patterned with the electrode channels was stacked above a thin layer patterned with the sample channel. The thin layer provided a built-in membrane to separate the two layers. To fabricate the layers, liquid polydimethylsiloxane was mixed in 10:1 ratio of elastomer to curing agent and degassed. In the case of the electrode channel layers, aluminum foil was wrapped around the edges of the silicon wafer to prevent spillage of PDMS. Liquid PDMS was poured onto the silicon wafer, which was cured by ramping the temperature to 60 ˚C for 5 minutes, 70 ˚C for 5 minutes, and 95 ˚C for 45 minutes. In the case of the thin sample channel layer, 2 g of liquid PDMS was poured in the center of the silicon wafer, which was spun on an in-house spin coater for 2 minutes. The thickness of the membrane was previously determined to be approximately 20 µm. for these conditions. The thin layer was cured by a temperature ramp of 60 ˚C for 5 minutes, 70 ˚C for 5 minutes, and 95 ˚C for 15 minutes. For both layers, the hot plate was then turned off and the wafer was allowed to

cool down on the hot plate to room temperature (about 20 minutes). The aluminum foil was peeled off the wafer and the solid PDMS was removed, trimmed of excess. Access holes were punched in the inlet and outlet of the channels using a 1.5 mm core sample cutter (Harris Uni-Core, Ted Pella, Inc., Redding, CA, USA). The electrode channel side was cleaned using Scotch Magic tape (3M, St. Paul, MN, USA). The electrode channel layer and the wafer-thin layer assembly were placed in an air plasma cleaner (Harrick Plasma, Ithaca, NY, USA). The layers were exposed to plasma for 6 minutes, after which the electrode layer was bonded channel-side-down to the thin PDMS layer on the wafer. The assembly was heated for 15 minutes (5 minutes at 60 ˚C, 5 minutes at 70 ˚C, 5 minutes at 95 ˚C). The hot plate was turned off and the assembly was allowed to cool to room temperature. A surgical blade was used to gently cut the thin layer around the edges of the bonded device, avoiding scratching the silicon wafer. The assembled device was slowly peeled off of the wafer, access holes were punched in the inlet and outlet of the sample channel, and the channel side was cleaned using tape. The bilayer device and a glass microscope slide (Premiere, China) were exposed to air plasma for 2 minutes and bonded together. Devices were stored under vacuum until use.

4.4 Experimental Characterization of Dielectric Properties of MOSE Cells Treated with Exogenous Sphingolipids

4.4.1 Low Frequency cDEP Device Layout

Continuous sorting single-layer cDEP devices pioneered by Sano *et al.* [75] were utilized for a cell study to assess the effects of non-toxic doses of sphingolipid metabolites on the dielectric properties of progressive stages of MOSE cells. The microdevice used in the experiments (Figure 7) consists of a straight main channel flanked by parallel fluid electrode channels, each 50 μm in depth. The main channel possesses a series of rounded ‘sawtooth’ features that constrict the main channel from 500 μm width to 100 μm between the inlet and outlet. These sawtooth features create high electric field gradients in the channel constrictions, and the series of six features increases the length of time that the cells are exposed to the DEP force, enhancing the observed translational motion of the cells. Fluidic electrode channels are separated from the sample channel by 20 μm

thick insulating barriers that run parallel to the sample channel for 6 mm and are identical height to the channel.

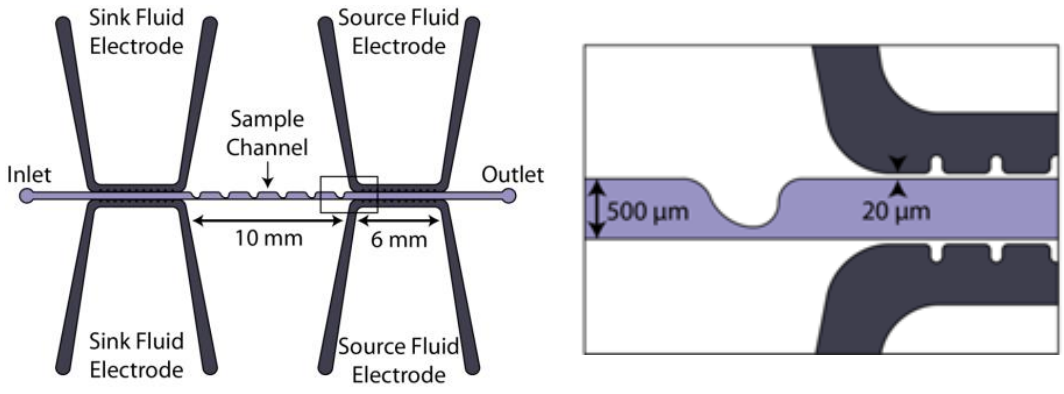

Figure 7. Schematic of low frequency cDEP device used for characterization of MOSE cell properties. Dimensions are noted on figure. Inset is detail of the final sawtooth feature in the series and electrode channels. The constriction width is 100 µm. Sink fluid electrodes are connected by a wire electrode, and source fluid electrodes are connected by a second wire electrode. The sample is pumped from the inlet to the outlet.

The electric field distribution and shear rate through the sample channel were first computationally modeled by Sano *et al.* [75]. The constrictions in the channel introduce non-uniformities in the electric field and cells can be directed to the top of the channel by positive dielectrophoresis or to the bottom of the channel by negative dielectrophoresis. The shear rate increases in these constricted regions but remains below the threshold for cell lysis.

4.4.2 Cell Culture and Experimental Setup

MOSE cells were cultured in high glucose DMEM (Sigma Aldrich) supplemented with 4% fetal bovine serum (Atlanta Biologicals), 3.7 g/L NaHCO3, and 1% penicillin/streptomycin (Sigma Aldrich). MOSE-E and MOSE-L cells were treated with 1.5 µM So or 500 nM S1P as BSA complexes (BSA, fatty acids-free fraction V, Calbiochem) for three passages, allowing 3-4 days between each passage. These treatments were not toxic to the cells.

MOSE cells were harvested by trypsinization, and washed and resuspended in DEP buffer (8.5% sucrose [wt/vol], 0.3% glucose [wt/vol], 0.725% RPMI [wt/vol]) [46] to a

concentration of 3×10^6 cells/mL. The cells were stained with Calcein-AM (Molecular Probes Inc., Carlsbad, CA, USA), at a concentration of 2 µL dye per mL cell suspension. The final cell suspension had an average conductivity of 96.97±4.15 µS/cm, measured with a conductivity meter (Horiba B-173 Twin Conductivity/Salinity Pocket Testers, Cole-Parmer).

The PDMS device was placed under vacuum for 30 minutes immediately prior to priming the main channel with the cell suspension. The main channel was primed with the cell suspension introduced to the main channel inlet through tubing attached to a syringe with a needle tip (Cole-Parmer Instrument Co., Vernon Hills, IL). Pipette tip reservoirs were inserted into the fluid electrode channel inlet and outlet, and the fluidic electrode channels were filled with phosphate-buffered saline (PBS) solution of conductivity 1.4 S/m. Aluminum wire electrodes were inserted into the fluidic electrode reservoirs. After priming, the device was transferred to the stage of an inverted light microscope (Leica DMI 6000B, Leica Microsystems, Bannockburn, IL) and a syringe pump supplied a pressure-driven flow rate of 0.005 mL/hr (PHD Ultra, Harvard Apparatus, Holliston, MA, USA) for cell characterization experiments in the low-frequency cDEP devices.

To generate the AC electric field, the output signal from a function generator (GFG-3015, GW Instek, Taipei, Taiwan) was amplified (Model 2205-CE, Trek, Medina, NY, USA) to produce output voltages ranging from 0-200V_{RMS} at frequencies between 5 and 70 kHz. Voltage and frequency were monitored using an oscilloscope (U2701A, Agilent, Santa Clara, CA, USA) connected to the output of the function generator.

(a) **(b)**

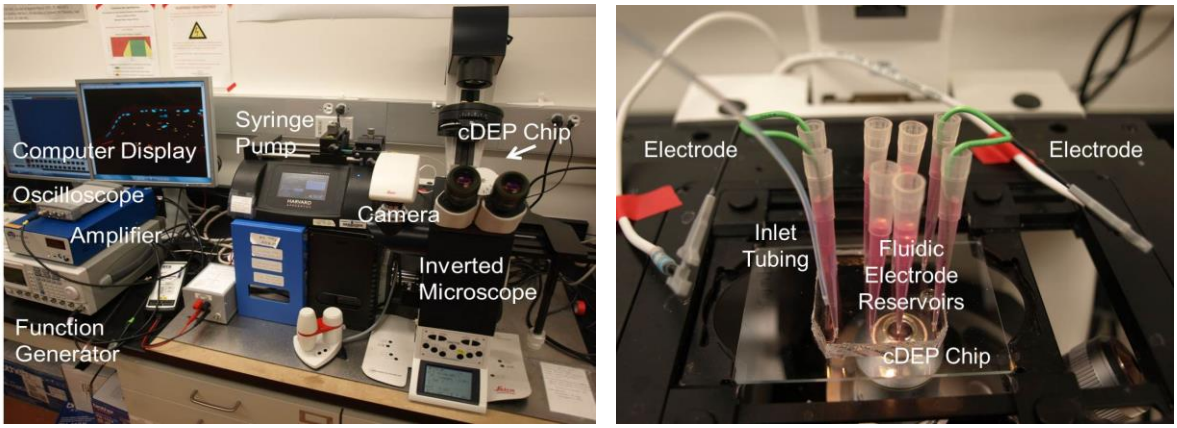

Figure 8. (a) Overall experimental setup, including high voltage electronics, syringe pump, inverted microscope, and cDEP chip. (b) Detail view of the cDEP chip on the microscope stage, showing fluidic and electronic connections.

Conducting experiments on the stage of an inverted microscope equipped with a camera allowed real-time monitoring of cell response. Leica Application Suite 3.8 software (Leica Microsystems, Bannockburn, IL, USA) was used for recording videos of cell movement at systematically varied frequencies. Frequencies at 2.5 kHz intervals were varied randomly during characterization experiments for a given voltage and flow rate. Image processing was accomplished using an in-house MATLAB (R2012a, MathWorks Inc., Natick, MA, USA) script. For each two minute video, the spatial distribution of cells through the sample channel was determined by recording the y-position of each cell as it passed a superimposed vertical line (Figure 13) The centerline of each distribution was then compared to the average centerline of control cell distributions in which no electric field was applied, and the crossover frequency was determined by interpolation.

4.5 Numerical Modeling for Predicting Performance of a New cDEP Multilayer Device for Cell Sorting

4.5.1 Layout for Multilayer Device with Curved Interdigitated Electrode Channels

New devices were designed with the objective of achieving cell sorting for 2 or more cell populations. These designs utilized a multilayer fabrication technique in which fluidic electrodes overlaid the sample channel, and were separated by a thin layer of PDMS acting as an insulating barriere. Here, Table 1 and Figure 9 present the fixed geometric

parameters used in the model.

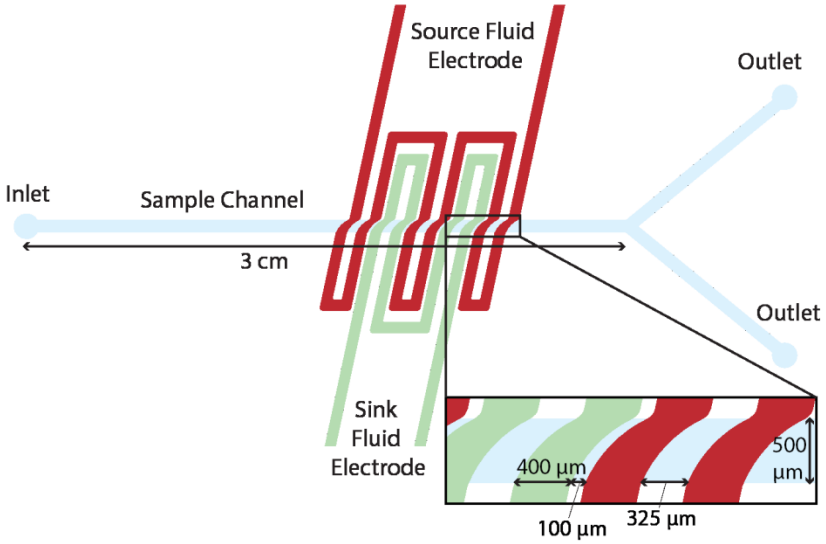

Figure 9. A multilayer cDEP device with 45˚ curved interdigitated source (red) and sink (green) electrodes, of 4:1 electrode width to gap width ratio, is shown with a detailed inset of the electrode channel curves. The sample channel (blue) spans 3 cm from inlet to the outlet branches, with 500 µm width (inset) and 50 µm depth. The electrode channels are 400 µm wide with slight narrowing across the curve.

A 20 µm thick barrier layer was used to minimize the voltage drop across the insulating barrier [79]. The sample channel and electrode channel depths were prescribed to be 50 µm to allow easy fabrication of these devices from SU-8 photoresist etched on a typical silicon wafer in a clean room, using the process described in Multilayer Device Fabrication Section 4.3. However, this depth can easily be increased by using fabrication processes such as hot embossing or injection molding to create the polymeric cDEP device, or by specially etching thick silicon wafers. A consistent spacing of 325 µm between pairs of ground and source electrodes was used. The nominal ratio of electrode width to gap width refers to the ratio of the widths of one electrode channel to the gap between one source and one ground electrode. The electrode-to-gap width ratio is nominally determined by the width of the channels at the base of the curved portion, which is 500 µm below the centerline of the electrode channels.

Table 1.Fixed geometric parameters and dimensions

Fixed Parameter	*Value*
Barrier thickness [µm]	**20**
Electrode channel depth [µm]	**50**
Spacing between pairs of electrodes [µm]	**325**
X-offset between bottom and top of curve [µm]	**1) 500**
Y-distance of curve [µm]	**500**

4.5.2 Numerical Modeling

A 3D finite element model of the new devices was constructed and solved to predict device performance. The device geometry was drawn using AutoCAD and imported into COMSOL Multiphysics 4.3a (Comsol Inc., Burlington, MA, USA). DEP force was predicted using the Electric Currents module. Table 2 presents the values of electrical conductivity and permittivity used in the computational modeling. PBS properties were applied to the fluid electrode channels and DEP buffer properties were used for the sample channel. The electrical properties of PDMS used in the model have been reported by the manufacturer (Sylgard 184, Dow Corning, USA).

Table 2.Material properties assigned to the computational model

Parameter	*Value*
Conductivity of DEP buffer, σ_m [S/m]	0.01
Relative permittivity of DEP buffer, ϵ_m	80
Conductivity of PBS, σ_{PBS} [S/m]	1.4
Relative permittivity of PBS, ϵ_{PBS}	80
Conductivity of PDMS, σ_{PDMS} [S/m]	0.80e-12
Relative permittivity of PDMS, ϵ_{PDMS}	2.65
Permittivity, ϵ_0 [F/m]	8.854187817e-12

The modeled microdevices consist of a straight main channel and overlaid interdigitated fluid electrode channels. The main channel and the height and width can be tailored for

the desired throughput or application. The overlaid electrode channels consist of curved geometry. These channels are separated from the main channel by a 20 μm thick insulating layer of PDMS. The width of the curve tapers slightly from the bottom side of the channel to the top side. This geometry can be tailored to achieve a desired DEP force given a particular frequency by changing parameters such as the angle of curvature, nominal ratio of electrode width to gap width, and number of electrode pairs in series. The nominal ratio of electrode width to gap width is determined by the distances at the bottom of the channel.

To predict optimal device performance, a parametric study was conducted on the angle of the curve, the ratio of the electrode width to the gap width between an interdigitated source and ground electrode pair, as well as the number of electrode pairs. The angles of 35˚ to 65˚ by intervals of 5˚, ratios of 1:1, 2:1, 3:1, and 4:1 were studied, and 4, 6, 8, 10, 12 electrode pairs were studied (Table 3). While a 2D model could be used, a 3D model was chosen given the multi-layer structure of the device, to avoid potential errors arising from assigning boundary conditions especially at the thin insulating layer between the electrode channels and the sample channel. The 3D simulation was performed using the Electric Currents module of Comsol Multiphysics 4.3 (Comsol Inc., Burlington, MA, USA). A 3D rectangular block was generated in the Geometry node, and assigned as the sample channel. A second 3D block was generated to serve as the surrounding chip material, and given dimensions much larger than those of the sample channel. A 2D electrode geometry generated in Autocad (Autocad 2012—Student Version, Autodesk Inc, San Rafael, CA, USA) was imported to a work plane located above the sample channel block. The vertical distance between the work plane and the ceiling of the sample channel was equal to the barrier thickness, 20 μm. The imported 2D geometry was extruded to a depth of 50 μm. The large block was assigned the material properties of PDMS, the sample channel was assigned the properties of the sugar solution used as the low conductivity buffer, and the electrode channels were assigned the properties of PBS. Current conservation boundary conditions were applied to all domains. Electric insulation boundary conditions were applied to the edges of the PDMS block. An electric potential of 100 V was applied to each inlet of the upper electrode channel. A ground boundary

condition was applied to each inlet of the lower electrode channel. Due to the AC signal, the potential can be applied to either electrode. A free tetrahedral mesh with three sizes was created. The size of mesh for the sample channel was "Extremely Fine," the electrode channels were "Extra Fine," and the surrounding PDMS domain was "Finer." The resolution of the mesh was increased in the regions where greater accuracy was desired in order to better predict the gradients in the sample channel. Using lower resolution mesh far from the sample channel decreased the time required to solve the model.

The frequency was swept from 0 Hz to 500 kHz at 5 kHz intervals. A surface plot of $\nabla(E \cdot E)$ in the sample channel was generated for a horizontal cut plane 15 μm below the interface of the barrier and the sample channel (z = 35 μm). Cut lines located at the same depth as the cut plane were also drawn. Line plots of $\nabla(E \cdot E)$ vs. x-coordinate were generated near the top edge of the channel (y = 200 μm), along the center of the channel (y = 0 μm), and near the bottom edge (y = -200 μm). Additionally, the potential drop and electric field were plotted vs. x-coordinate for the center cut line.

To optimize the design, the performance of devices with parametrically varied electrode geometries was predicted by the method described above. Unique geometries were created by changing one parameter at a time while holding the others constant: angle of curvature of electrodes, electrode width-to-gap width ratio, and number of electrode pairs.

The angle of curvature refers to the enclosed angle of the arc forming the curved portion of the electrode channel. The arcs spanned a 500 μm x-distance along the channel and a y-distance equivalent to the width of the sample channel. Modeling was done for arcs with endpoints at the edges of the sample channel prior to filleting the corners. For fabrication purposes, masks were made in which the arc endpoints extended past the edges of the sample channel. This design was more forgiving of slight alignment mismatches, and has the added benefit of avoiding sharp corners and thus extremely high regions of DEP force in the channels.

Table 3. Parameters for device optimization study

Parameter	*Values*
Angle of curvature	35, 40, 45, 50, 55, 60, 65, 80
Electrode width-to-gap ratio	1:1, 2:1, 3:1, 4:1
Number of electrode pairs	4, 6, 8, 10, 12

Using the Electric Currents (frequency domain) module, electrical insulation boundary conditions were applied to the four edges of the PDMS block and current conservation boundary conditions were applied to all domains. An electric potential of 100 V was applied to the tips of one fluidic electrode channel and the ground condition was applied to the tips of the other fluidic electrode channel. A finite element mesh was generated by assigning three different free tetrahedral sizes to distinct domains. Because the solution accuracy was most important in the sample channel, this domain was meshed "Extremely fine." Due to the small feature sizes of the electrode channels but less need for accuracy, they were meshed "Extra fine," and the PDMS block was meshed "Finer" to avoid a drastic mismatch between mesh sizes at the interface with the channels. Though still a relatively fine mesh, this size is coarser than that of the other domains and the settings have a built-in element growth rate that allows elements to become larger far from the small features to allow more rapid solving. A box for selectively refining the mesh in the center of the sample channel was bounded from x = [-3525, 3525], y = [-250, 250], and z = [-25,100]. A mesh resolution study was performed in the bounds of this box to ensure that mesh size did not affect the solutions of electric field and $\nabla(E \cdot E)$. The mesh was refined from 1 to 6 times . Increasing the number of refinements had little effect on the solution of the electric field, which appeared to converge even at one refinement (Figure 10). While even one refinement yielded a converged solution for $\nabla(E \cdot E)$ at the majority of positions along the channel (Figure 11), some variation was observed at the maxima.

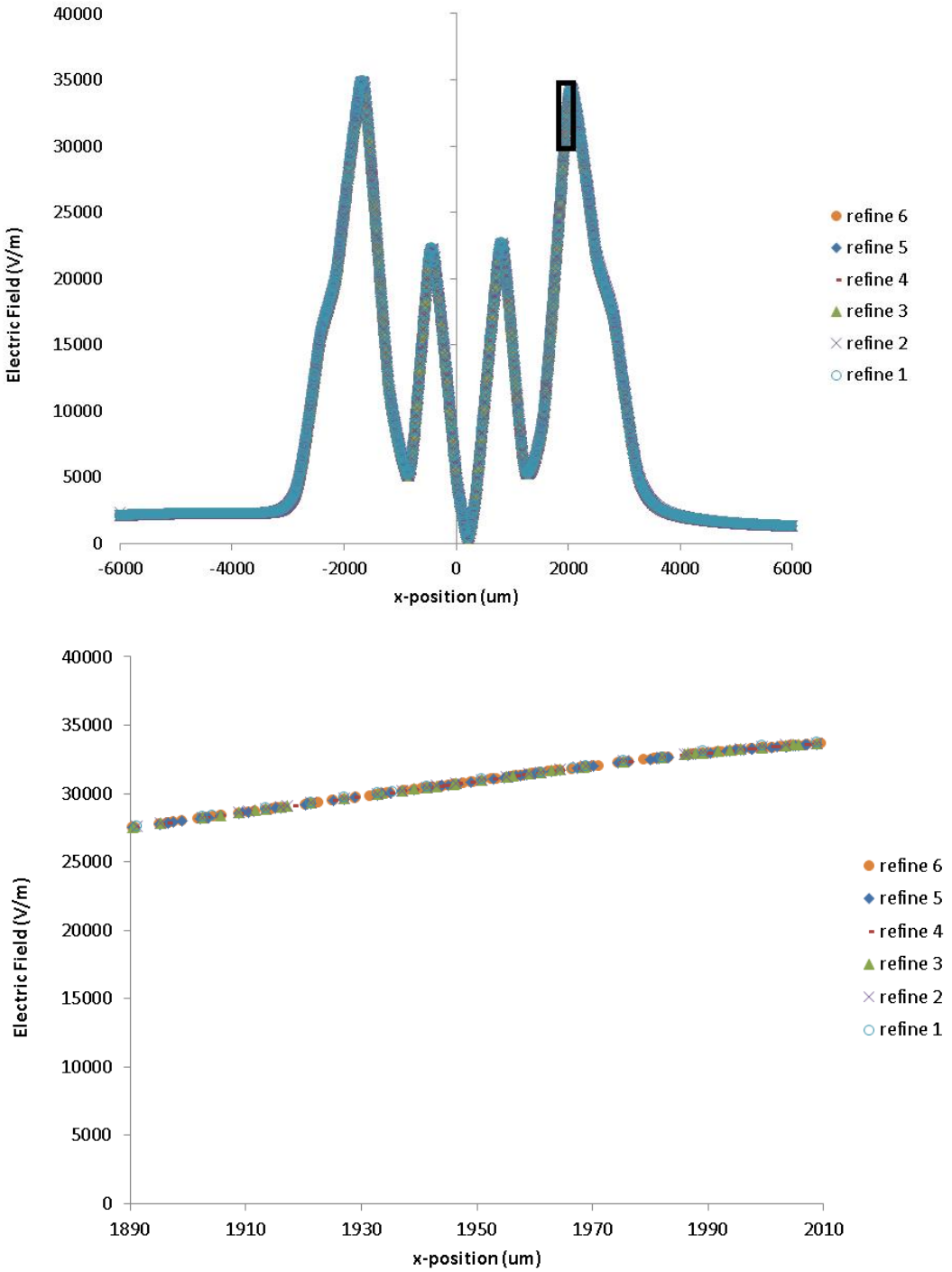

Figure 10. (a) The solution for the electric field at 100 kHz along the sample channel, down the x-centerline, 15 µm below the channel ceiling. The mesh was refined up to 6 times in a box surrounding this region of the sample channel. The black box represents the region presented in (b), a detail view of the solution near a peak in the electric field, demonstrating good convergence at all levels of refinement.

Based on the lack of a discernible difference between each level of refinement (Figure 10 above), this mesh resolution study would indicate that even one level of refinement is

sufficient to generate an accurate solution. To further explore the effect of mesh refinement on the predicted DEP force in the channel, the same study was performed for $\nabla(E \cdot E)$ (Figure 11).

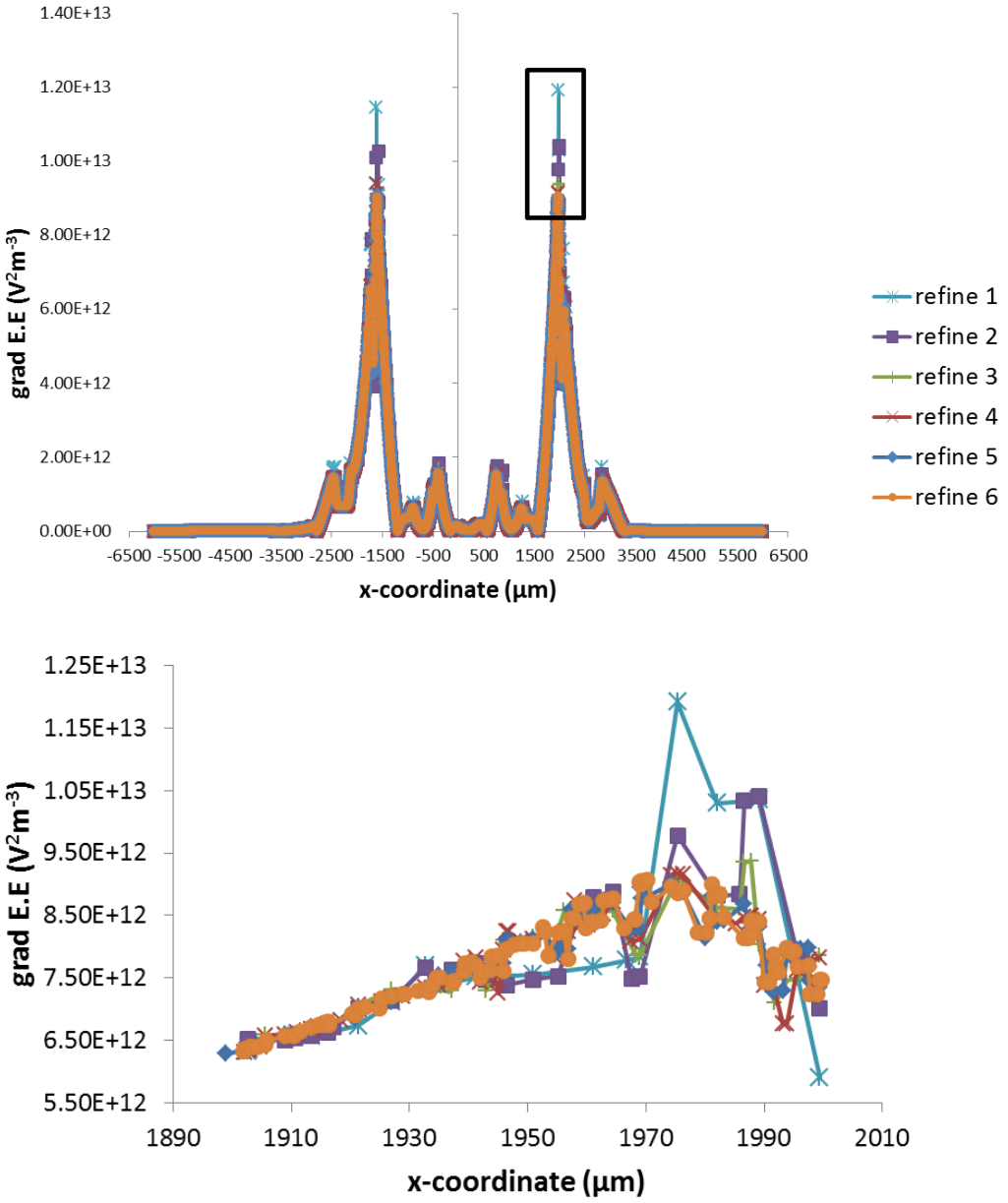

Figure 11. A mesh resolution study was performed for 1-6 refinements and plotted along the centerline of the channel shows that (a) the most variation occurs in the peak regions and detail (b) shows that the solution begins to converge after 3 refinements.

Again, strong convergence was demonstrated for most points along the sample channel, but the most variation was apparent in the peak regions. To yield a rough determination

of which level of refinement was sufficient for accuracy, the solutions for $\nabla(E \cdot E)$ at a maximum were examined. The average percent difference between three values of $\nabla(E \cdot E)$ at identical x-coordinates for each refinement was calculated (Table 4), as well as the average percent difference from the value provided by six refinements. A model with seven refinements generated over 25 million elements with over 34 million degrees of freedom, but required over 120 hours to solve, so the results were not included here.

Table 4.Statistics for mesh refinement study on $\nabla(E \cdot E)$.

# refinements, r	Number of elements, N_E	Number of degrees of freedom, dof	Time to solve, t (hr:min:sec)	Average % error from values at 6 refinements in peak region	Average % change from one refinement to the next highest level
1	933,679	1,268,330	00:58:42	25	12
2	1,097,144	1,488,823	01:06:37	11	13
3	1,461,556	1,988,420	01:30:14	2.7	1.2
4	2,445,778	3,315,782	03:17:08	1.5	1.7
5	4,777,431	6,510,144	05:31:23	3.3	3.4
6	11,394,015	15,445,076	15:03:10	n/a	n/a

Three refinements were deemed sufficient due to the 1.2% average change from three to four refinements in the region of highest variability, the maximum peak of $\nabla(E \cdot E)$. There was a larger percent change from five to six refinements than from previous levels to the next highest, and a larger percent difference from the value at six refinements. However, these values were only taken for an average of points in a region with the most noise, meaning that they do not reflect the overall increase in accuracy throughout the entire region, and serve as a rough measure for differentiating between already-accurate solutions. Given the convergence of the solutions for the electric field from even one refinement, taking three refinements simply adds additional accuracy to the solutions.

The percent "error" from six refinements was only 2.7% for three refinements. Given that six refinements required over 10 times the amount of time required to solve for three refinements, and that three refinements provided a close match for all values, with less than 3% difference from the values obtained at six refinements and about 1% difference

from the next level of refinements (four), three refinements was chosen as the optimal mesh resolution.

4.6 Preliminary Validation Studies of Multi-Stream-Sorting cDEP Devices

Murine prostate cancer (PC3) cells were cultured in growth medium (RPMI 1640 with L-glutamine, 10% FBS, 1% penstrep) and suspended in low conductivity buffer as described in Section 4.4.2 Cell Culture and Experimental Setup. Multilayer devices were fabricated as described in Section 4.3 and prepared as described in Section 4.4.2. Cells were pumped continuously through the sample channel at 0.005 ml/hr and the voltage and frequency were adjusted to qualitatively observe the DEP response of the cells. The device was tested between 0-100 V and 70-500 kHz because computational modeling predicted sufficient $\nabla(E \cdot E)$ at 100 V and high frequencies. Videos and images were recorded of cell motion. A schematic of the setup is presented in Figure 12.

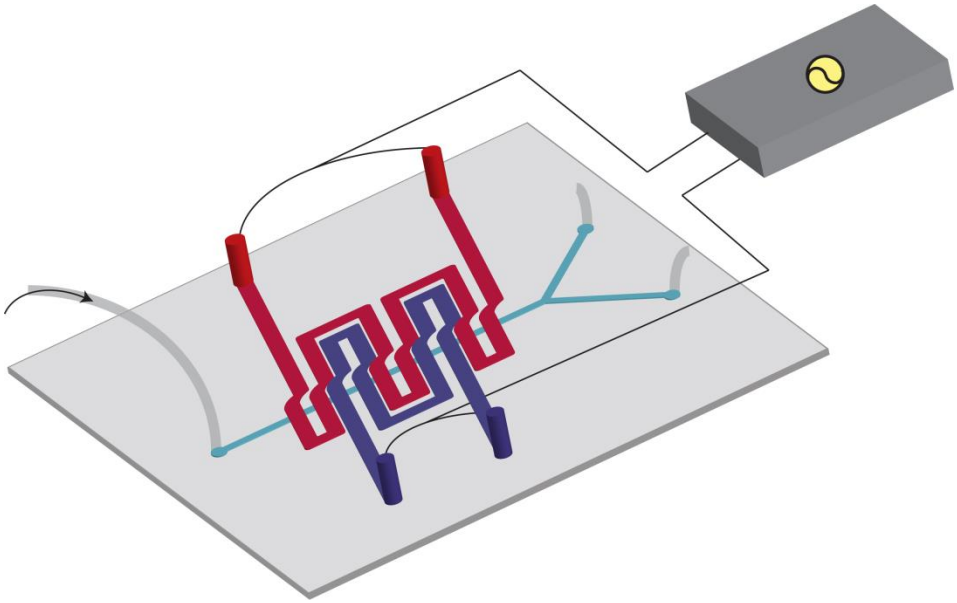

Figure 12. The multilayer cDEP device was connected to high voltage electronics at the source (red) and sink (purple) electrode channels, and the cell suspension was introduced to the sample channel (blue) by pressure-driven flow at the inlet (denoted by arrow). Cells can be collected at the outlet in tubing reservoirs. The chip was placed on an inverted microscope for imaging cell movement.

Chapter 5: Results and Discussion

5.1 Detecting a Shift in Electrical Properties of Aggressive Ovarian Cancer Cells in Response to Non-toxic Doses of Sphingosine

5.1.1 DEP Response of a Mouse Ovarian Surface Epithelial Cell Syngeneic Model

Figure 13 illustrates cell movement in the sample channel without any applied electric field, and due to applying 200 V_{RMS} and at frequencies lower and higher than the crossover frequency [117]. As was shown in the computational results, $\nabla(\vec{E}_{RMS}.\vec{E}_{RMS})$ is much greater at the top side of the channel due to the sawtooth features, which induce non-uniformities into the electric field. When applying a frequency less than the first crossover frequency of cells, cells experienced a negative DEP force and were repelled from the sawtooth features, resulting in deflection towards the bottom half of the channel. However, when applying a frequency higher than the first crossover frequency, cells experienced pDEP force and were attracted towards the sawtooth features and the top side of the channel. Figure 13d, 13e, and 13f demonstrate the normalized cell distribution corresponding to no DEP force from Figure 13a, nDEP from Figure 13b, and pDEP from Figure 13c, respectively. Figure 13d shows the distribution of cells without an applied voltage to verify that the cells were randomly distributed in the absence of an electric field. Cell distributions were normalized by the total number of cells crossing the red line in Figure 13 to allow comparisons of cell distributions in different experiments since the total number of cells was not precisely the same in each experimental run. The results presented in Fig 13b and c are in agreement with the computational modeling of the trajectories of particles at 5 and 20 kHz [117].

5.1.2 Extracting Dielectric Properties of MOSE Cells

The average crossover frequency for the benign MOSE-E and malignant MOSE-L cells under each treatment condition was calculated. Since the conductivity of each cell sample was slightly different, the crossover frequency from each experiment was divided by the sample conductivity in that experiment, based on the linear relationship between

conductivity of the sample and crossover frequency (Equation (3.22)). These values, f_{xo}/σ_m, were compared by a student t-test. The ratio of crossover frequencies to sample conductivity, f_{xo}/σ_m, for untreated, So-treated, and S1P-treated MOSE-E cells were not statistically different, indicating that exogenous sphingolipids do not affect the crossover frequencies of MOSE-E cells (Table 5) [117]. Under identical treatment conditions, f_{xo}/σ_m of MOSE-L cells doesed with So increased to 1.94±0.07 from the untreated value of 1.35±0.14 MHz·m/S, and was significantly higher than f_{xo}/σ_m of control or S1P treated MOSE-L cells ($p<0.001$). Importantly, there was no statistically significant difference between f_{xo}/σ_m of So-treated MOSE-L cells and control MOSE-E cells ($p=0.29$), indicating that So treatment effectively reversed the crossover frequency of MOSE-L cells to that observed in MOSE-E cells. Additionally, the crossover frequency of MOSE-L cells did not change after the treatment with S1P, indicating that the change in electrical properties was specific to dosing with So, rather than a generic reaction to sphingolipid treatment or possible metabolism of So to S1P [117].

Table 5.Dielectric properties of MOSE cells treated with sphingolipids

Cell type and treatment	***Normalized crossover frequency (MHz·m/S)***	***Specific membrane capacitance (mF/m^2)***
MOSE-E untreated	1.96±0.16	16.05±1.28
MOSE-E SO	2.06±0.18	15.26±1.38
MOSE-E S1P	2.00±0.39	16.15±3.55
MOSE-L untreated	1.35±0.07	23.94±2.75
MOSE-L SO	1.94±0.07	16.46±0.62
MOSE-L S1P	1.21±0.14	26.89±3.91

Given the conductivity of the media and the known crossover frequency and radius of the cells, the specific membrane capacitance, C_{mem}, was be calculated using Equation (3.22). Neither So nor S1P treatment caused a significant change in C_{mem} of MOSE-E cells. The specific membrane capacitance of MOSE-L cells was significantly higher ($p<0.01$) than MOSE-E cells; treatment with So, however, significantly decreased C_{mem}

to the levels of MOSE-E cells while S1P treatment was not associated with a change in C_{mem} of MOSE-L cells (Table 5) [117]. As in the case of the normalized crossover frequency, these results indicate that the decrease in C_{mem} is specific for So treatment of aggressive cancer cells and that benign cells are not affected. The measured radius of 7.185±1.004 and 7.050±1.195 μm of MOSE-E and MOSE-L cells, respectively, were used to calculate C_{mem}.

. The difference in electrical phenotype of MOSE-E and MOSE-L cells confirmed previously reported cDEP studies by Salmanzadeh *et al.* [76]. This distinction is hypothesized to arise at least in part from the biophysics reported by Ketene *et al.*, indicating that MOSE-E cells were mechanically stiffer than MOSE-L cells due to more organized actin filaments [109, 118].

The most important finding of this study was that non-toxic doses of sphingosine were linked to a reversal in the electrical phenotype of MOSE-L cells to that of MOSE-E cells. Babahosseini *et al.* reported a 30% increase in elasticity of MOSE-L cells upon treatment with 1.5 μM So for 3 passages [119], which suggested that So reversed the biomechanical properties of aggressive MOSE cells. By demonstrating that So also reversed crossover frequency and thereby the calculated specific membrane capacitance of MOSE-L cells, we have shown that cDEP is useful to detect cytoskeletal reorganization of cells, without the need for labeling or fixing cells, or performing serial analytical methods. This was the first demonstration of cDEP for interrogating metabolite-induced changes in the biophysics of a particular cell type.

Sphingosine-1-phosphate was chosen as a contrasting treatment because of its prevalence in the ascites fluid surrounding ovarian tumors, as well as a control to determine if the effects of sphingosine were generic to other sphingolipid treatments. With respect to the sphingosine-1-phosphate control, it might be expected that S1P treatment of MOSE-E cells would be linked to dielectric properties similar to aggressive MOSE-L cells because S1P is generally a tumor-promoter. However, S1P had little or no effect on the dielectric properties of MOSE-E cells measured here. We suggest that this finding is analogous to

the results of Wang *et al.*'s study [25] on the effects of S1P and So on migration and morphology of epithelial ovarian cancer (EOC) cells and normal human ovarian surface epithelial (HOSE) cells. Their study indicated that S1P inhibited migration of normal HOSE cells while stimulating migration of EOCs. They also noted that increased filopodia-like features were found in the S1P-treated EOCS but not the normal HOSE cells, and that stress fibers were enhanced in S1P-treated HOSE cells. The study results imply that S1P does not have a monolithic effect on benign and cancerous ovarian cells; rather, S1P actually supported cytoskeleton organization and prohibited migratory effects in normal cells while increasing migratory-associated morphology and behavior in cancerous cells.

These intriguing results lead us to consider that a similar effect might occur in the MOSE-E and MOSE-L cells explored in our study; S1P might fail to induce cytoskeleton dysregulation or filopodia in MOSE-E cells, while increasing the already-aggressive features of MOSE-L cells, thus resulting in little to no detected change in the dielectric properties in either the MOSE-E or MOSE-L cells upon S1P treatment. Further supporting our hypothesis is that the S1P dosages in the two studies were similar: the 500 nM dosage used in our study falls in the middle of the 0.01-1 µM S1P concentration range studied by Wang *et al.* [25]. Further exploration of the effect of S1P on the migration and physiology of MOSE-E and MOSE-L cells should be conducted, specifically focusing on the effect of S1P on the actin fiber organization and membrane morphology. At present, we suggest that S1P acted as a negative control in comparison to So, reinforcing the conclusion that generic sphingolipid treatment does not result in monolithic changes in dielectric properties.

This experimental work demonstrated the potential of cDEP to be applied for drug screening applications that go beyond basic toxicity testing. By demonstrating that sphingolipid modulation therapy was linked to changes in dielectric properties of cells, we established a first step toward correlating the action of metabolites or drugs on the physical properties of cells with detectable changes in their dielectric signature and specific disease states. Importantly, no knowledge of surface biomarkers was required to

perform this screening. Independence from labeling is a key advantage when analyzing cancer cells, because treatments of interest may not act uniformly or significantly on expressed surface markers, making their effects invisible to traditional cell analysis techniques such as FACS or MACS. The potential of cDEP is powerful, as it can enable rapid analysis of alterations in the cytoskeleton of bulk populations of cells while maintaining viability, in contrast to time-consuming serial analysis of biomechanical properties by atomic force microscopy or imaging by immunofluorescence microscopy, which requires cells to be fixed. Future work will explore the potential for operating cDEP while utilizing the electrical phenotype as an indicator of treatment efficacy.

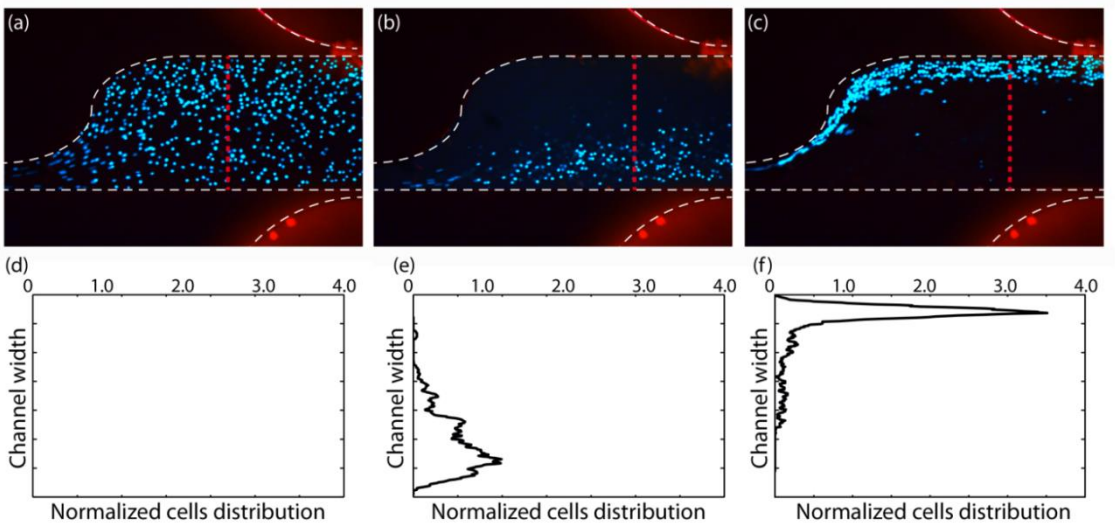

Figure 13. Determining crossover frequency of cells based on their movement towards top or bottom half of the channel. MOSE-L cell movement in the sample channel (a) remains uniformly distributed without applying any electric field, (b) shows nDEP due to applying 200 V_{RMS} at 5 kHz and (c) shows pDEP due to applying 200 V_{RMS} at 30 kHz. Normalized cell distributions corresponding to (d) no DEP force as in (a), (e) negative DEP as in (b), and (f) positive DEP as in (c).

5.1.3 Determining Effect of Buffer Type, Temperature, and Time on Diameter of Suspended MOSE-E Cells

During experiments, cells were suspended in DEP buffer, a sugar solution, for several hours. Because the DEP force acting on the cell is highly dependent upon cell size ($F_{DEP} \propto radius^3$), it was important to determine whether the buffer environment caused swelling or shrinkage of cells over time and whether cell size changed differently in DEP buffer than in a traditional 1X PBS solution. MOSE-E cells were studied as representative of the syngeneic MOSE cell line, and results are presented in Figure 14. No significant difference in cell diameter was found when comparing MOSE-E cells in

culture media, 1X PBS, and DEP buffer initially (at room temperature), and there was no significant difference in cell diameter after 5 hours for cells in 1X PBS versus DEP buffer that had been incubated (37 ˚C) or placed on ice (Figure 14). There was a significant difference in diameter after 5 hours at room temperature, where cells had an average diameter of 16.7 μm in 1X PBS and 16.3 μm in DEP buffer. The diameter of cells in 1X PBS was slightly closer to the average initial diameter of MOSE-E cells in culture media. However, for this condition, cell viability was much higher for cells in DEP buffer (92%) than in 1X PBS (82%).

These preliminary results suggest that for lengthy experiments around 5 hours, MOSE-E cells suspended in room temperature DEP buffer may reduce the diameter about 0.8 μm, which could reduce the DEP force to about 87% of its initial value, if all else is held constant. However, DEP buffer supports much higher viability than 1X PBS, as MOSE-E cells at room temperature after 5 hours were 92% viable, compared to 82% viable in 1X PBS (Figure 15). In experiments, any excess cell suspension for later use was maintained on ice, which was demonstrated to keep cell diameter the same. Additionally, most experimental runs lasted about 2 hours, less than half of the time at which a change in diameter was seen, and a freshly prepared cell suspension was used for most of the experimental runs, ensuring that cells were not fatigued by suspension and manipulation. Finally, these data suggest that DEP buffer did not induce any significant changes compared to PBS when cells were initially suspended, or when cells were kept on ice for 5 hours.

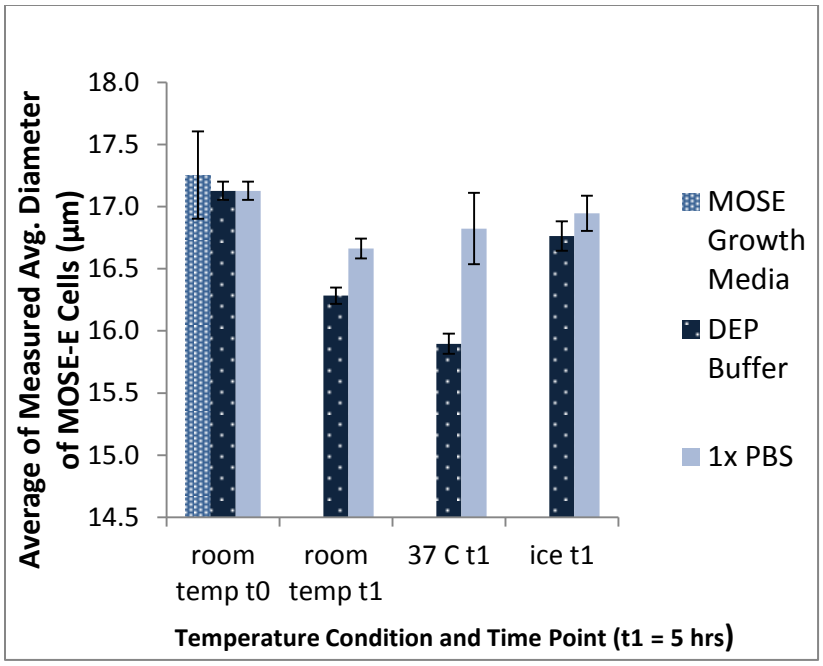

Figure 14. The average diameter of MOSE-E cell was measured for cells in low conductivity buffer, and 1x PBS at three different temperatures, over the course of five hours, and compared to the initial diameter of MOSE-E cells suspended in growth medium. The diameter of the cells in low conductivity buffer at the initial time point did not change from that of cells in normal growth medium. Also, the diameter of MOSE-E cells in low conductivity buffer on ice remained similar to that of the cells initially, while cells at room temperature decreased in diameter after 5 hours. This suggests that time and temperature of suspension have a greater effect on cell diameter than the low conductivity buffer itself.

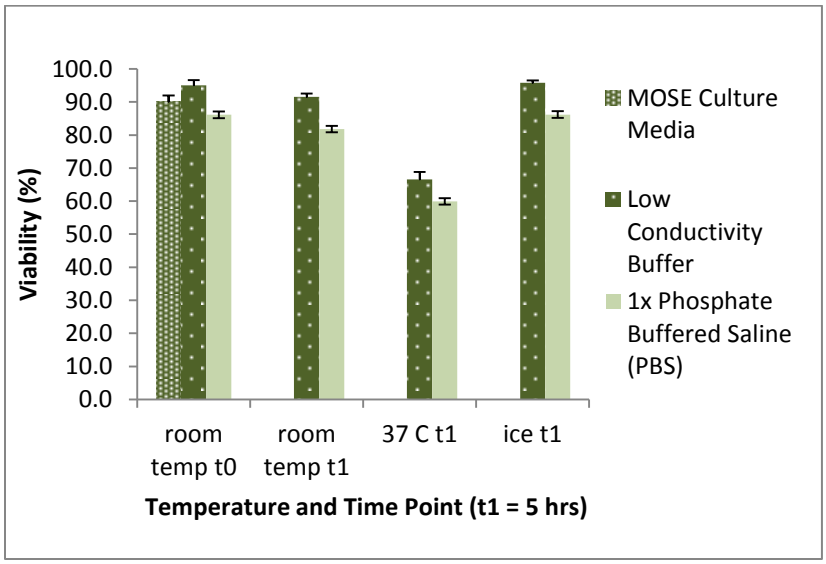

Figure 15. The viability of MOSE-E cells suspended in not adversely affected when suspended in low conductivity buffer at room temperature or on ice for 5 hours.

5.2 An optimized multilayer cDEP device with curved interdigitated electrodes for cell sorting

The original goal of performing a computational parametric study on angle of curvature, nominal electrode width-to-gap ratio, and number of electrode pairs was to determine the configuration that resulted in the maximum electric field gradients in the sample channel. The hypothesis was that increasing the angle of curvature would increase separation resolution of particles due to more varied angles of resultant forces, increasing nominal electrode width-to-gap ratio would increase DEP force farther from the electrodes, and that increased number of electrode pairs would increase the amount of time cells would be exposed to DEP force thus increasing separation resolution. Based on our optimization procedure, no detectable difference was found in magnitude or distribution of DEP force based on the angle, increasing the nominal electrode width-to-gap ratio did favorably increase the spatial distribution of DEP force, and increasing the number of electrode pairs above four failed to generate sufficient DEP force at the more central pairs of electrodes. Optimized parameters are presented in Table 6, and Figure 16 shows the distribution of $\nabla(E \cdot E)$ in the sample channel, in an xy-plane 15 μm below the channel ceiling.

Table 6. Optimized geometric parameters for multilayer cDEP device with curved interdigitated electrodes.

Optimized parameter	**Optimal Value**
Angle of curvature	No difference for angles between 35˚ and 65˚
Nominal electrode width-to-gap ratio	4:1
Number of electrode pairs	4

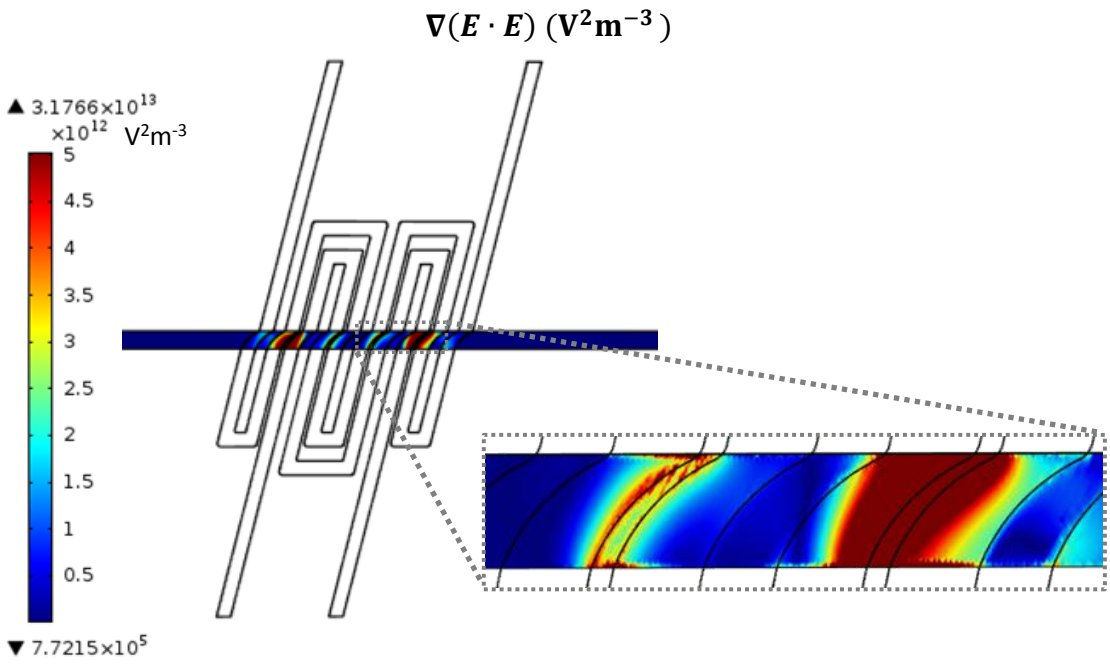

Figure 16. $\nabla(E \cdot E)$ is shown to be greatest in the gaps between a source and sink electrode as they cross the sample channel, with higher gradients occurring at the exterior electrode channel pairs. $\nabla(E \cdot E)$ surpasses the $1x10^{12}$ V^2m^{-3} threshold for cell manipulation by cDEP. The device shown has four electrode pairs with 45˚ included angle curves and a 4:1 electrode width-to-gap ratio.

Changing the included angle of the arc of the electrode channel failed to induce a significant change in the spatial distribution of the electric field, thus resulting in similar magnitudes of DEP force (Figure 17). However, the curve in the electrodes was limited by the endpoints being offset by 500 µm in the x- and y-directions and using a circular arc. Changing the form of arc to be more drastically curved, by using a different shape than a circular-based arc, or by extending x-distance between the endpoints of the endpoints of the curve, might lead to more drastic changes in the electric field distribution.

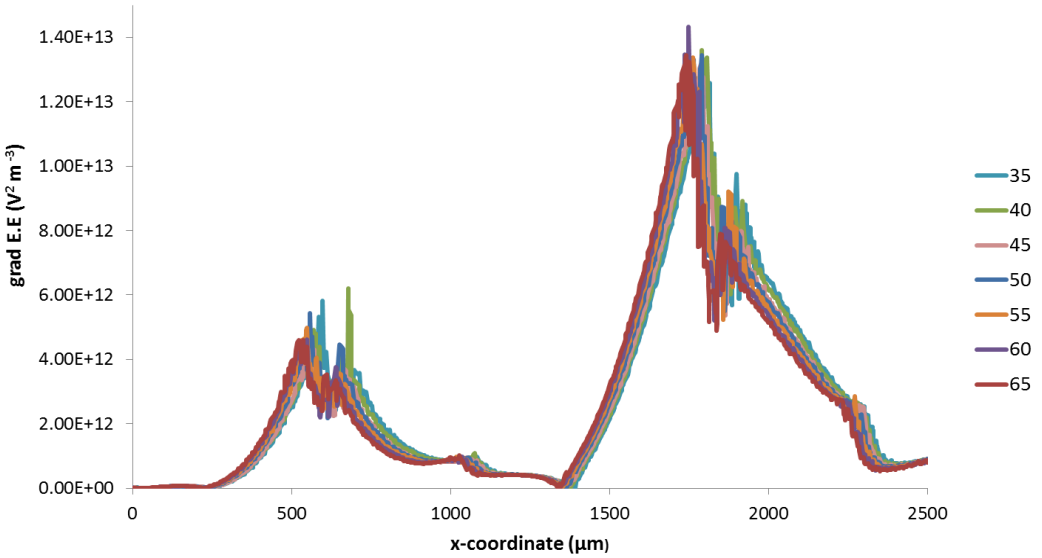

Figure 17. The magnitude of $\nabla(E \cdot E)$ generated along the centerline of the sample channel, 15 µm below the ceiling, at 100 V and 500 kHz does not significantly change with varied angles of curvature of electrode channels. As shown in the detail from x = [0, 2500], the region with the most apparent variation in $\nabla(E \cdot E)$, the distribution of $\nabla(E \cdot E)$ remains virtually the same but slightly shifts to higher x-values with lower angles of curvature. These simulations were run for the device having 4 electrode pairs and 4:1 electrode width to gap width ratio.

As the ratio of the electrode width to gap width increases from 1:1 to 4:1, $\nabla(E \cdot E)$ increases as well (Figure 18). This is in accordance with traditional dielectrophoresis devices that utilize interdigitated planar electrodes [36]. Electrode width in cDEP devices is constrained by the mechanical deflection of the PDMS ceiling of the electrode channel, as very wide channels may collapse. However, this issue was not observed with the 400 µm channels used here as the maximum width. Additionally, small supporting structures may be added to prevent collapse without detrimentally affecting the electric field generated.

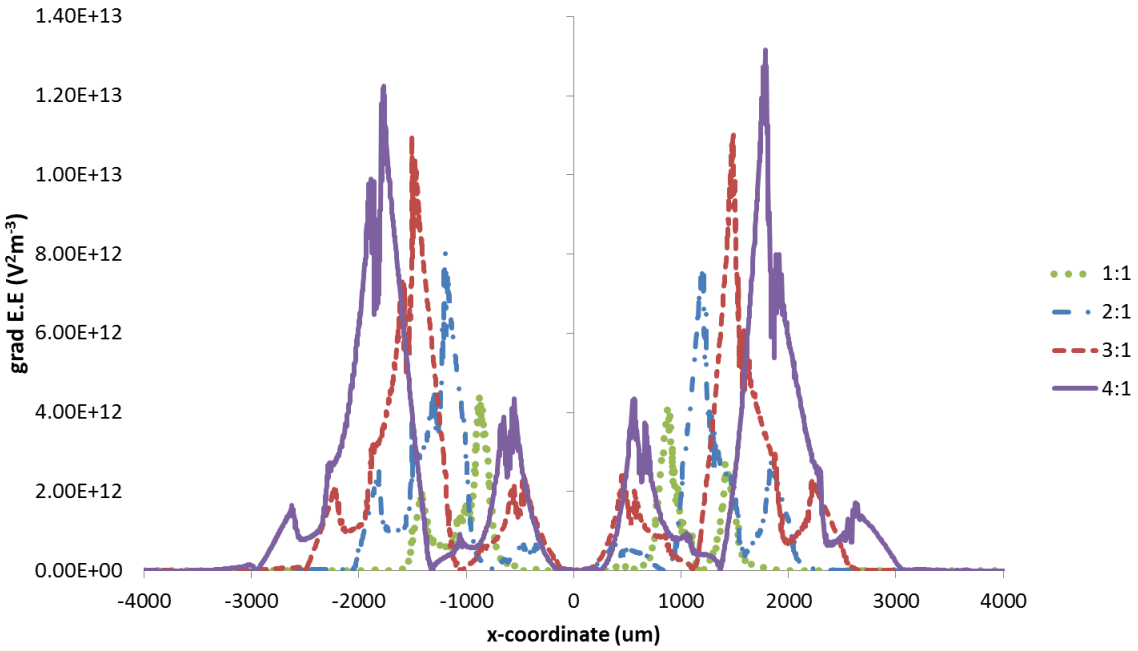

Figure 18. Increasing the electrode width to gap ratio increases the value of $\nabla(E \cdot E)$ in addition to expanding the area where $\nabla(E \cdot E)$ are sufficient for cell manipulation. These simulations were run for a device with 4 electrode pairs and 45 degree arcs.

The results of simulating devices with 4, 6, 8, 10, and 12 pairs of electrodes (Appendix B) indicated that sufficient DEP force is generated consistently at each pair of electrodes only when there are 4 pairs (Figure 19). Intuitively, it would be expected that more pairs of electrodes in series would expose cells flowing through the sample channel to DEP force for a longer time, which would result in increased separation resolution. In fact, this principle has been used in a previous low frequency design by Sano *et al.* where multiple sawtooth constrictions were placed in series [75]. However, for the interdigitated electrodes here, the channel length is much longer and the source and sink electrodes are much closer in proximity. The resistance of one electrode channel for even a 4 electrode pair configuration is on the scale of 1000 kΩ (Eqn 3.23-3.25). This high resistance leads to a significant voltage drop down the channel, which leads to the center pairs of electrodes having virtually equivalent voltage and no voltage drop between the "source" and "sink" electrode channels. The potential distribution is also frequency-dependent, and for the 4 pair case, above roughly 300 kHz, the potential distribution begins to flatten. Similarly, for the 8 pair case the potential distribution flattens above 100 kHz. The DEP force for the 8 electrode pairs is slightly higher at the edges than for the 4 pairs, due to the

slightly higher potential in that area. The reason for this could possibly be due to the increased spacing between the endpoints of the source electrode.

With virtually no voltage drop across the two channels, extremely low gradients of $\nabla(E \cdot E)$ result in insufficient dielectrophoretic force in those regions. Therefore, increasing the number of electrode pairs in this design is actually detrimental to cell sorting, because cells do not experience strong dielectrophoretic force through much of the length of the sample channel. However, increasing the depth of the electrode channel reduces the resistance, leading to higher $\nabla(E \cdot E)$ between the center pairs of electrodes. Additionally, the length of electrode channel can be reduced by sectioning the electrode channel into pieces and increasing the number of inlets.

$$R = \frac{\rho L}{A}$$

$$R \approx \frac{43400 * 10^{-6}\ \mu\text{m}}{\left(1.4\frac{\text{S}}{\text{m}} * (50 * 10^{-6}\ \mu\text{m} * 400 * 10^{-6}\ \mu\text{m})\right)} \tag{5.1}$$

$$R \approx 1550000\ \Omega \approx 1550\ k\Omega$$

Completion of this parametric study also suggests that optimizing for maximum electric field gradient is perhaps easier than expected, especially given the interdigitated electrode geometry used here. Studying the direction of the gradients and the trajectories of cell populations could elucidate the effects of changing the shape of electrodes more effectively than studying the maximization alone. Comsol offers a particle trajectory module that could be useful towards this goal. The predicted DEP force, drag force, and particle properties and distribution density can be input into the computational model to determine the direction of the particle motion.

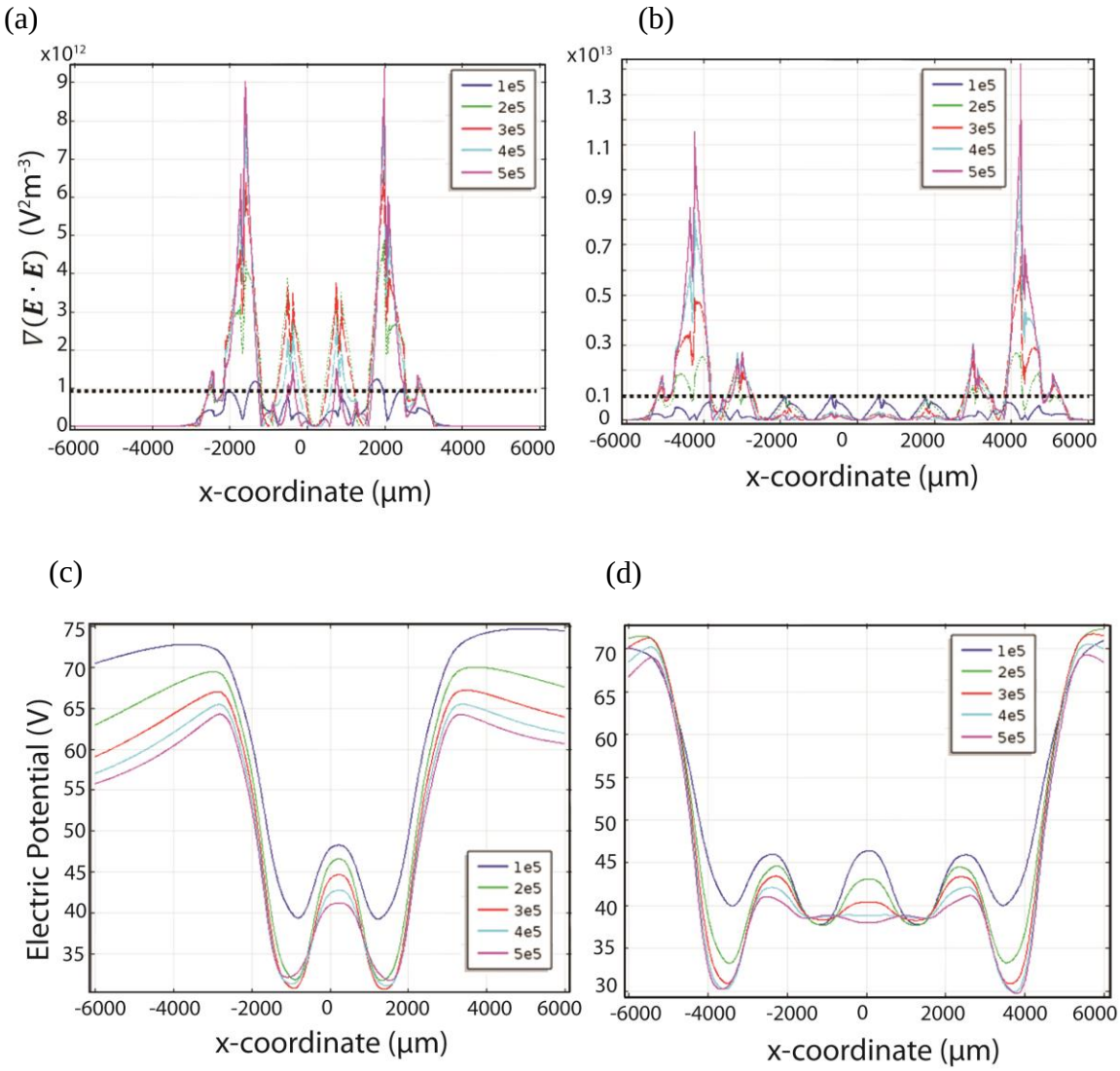

Figure 19. (a) The spatial gradient of the electric field potential distribution for 4 electrode pairs and (b) 8 electrode pairs is shown in (a), while the electric potential is shown in (c) for 4 electrode pairs and (d) 8 electrode pairs. As frequency increases, the potential distribution flattens in the center region of the 8 electrode pair device (d), resulting in little to no potential drop across electrode pairs and thus little to no DEP force as seen in (b). For the 4 electrode pair device, the potential does experience a flattening effect above 300 kHz (c), but sufficient DEP force can be generated above 100 kHz (a). Additionally, while there is a reduction in DEP force from the external electrode pairs to the central pairs , the reduction is less drastic than when 8 electrode pairs are modeled .

5.3 Results of Validation Experiments

The device was fabricated using identical dimensions to the model except for extending the arcs past the boundaries of the sample channel, which resulted in easier fabrication that was more forgiving in slight misalignment of the two layers, and also avoided

regions of high DEP force at the corner between the arc and the rest of the sample channel. The devices were tested between 0-100 V and 70-500 kHz because computational modeling predicted sufficient $\nabla(E \cdot E)$ at 100 V and high frequencies. Videos and images were recorded of cell motion. At 75 V and 300 kHz, cells were continuously deflected toward the top of the channel by positive dielectrophoresis (Figure 20). Under stronger electric fields, cells were trapped in long pearl chains at the top of the channel. In contrast, without the influence of an electric field, cells flowed straight through the sample channel with a uniform distribution across the entire width of the channel. These results indicate that these devices are useful for enriching cell populations.

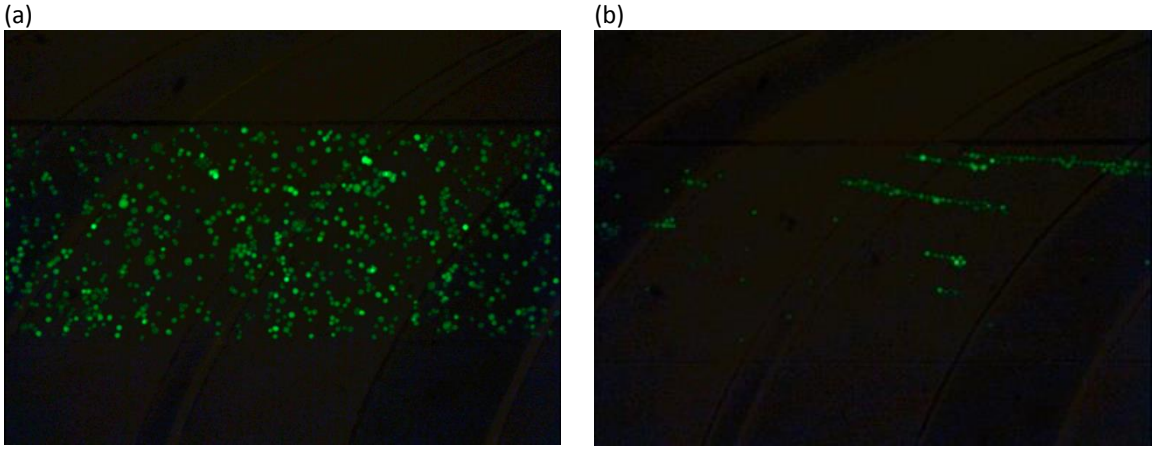

Figure 20 PC3 cells were flowed through the sample channel under various conditions. Fluidic electrode channels in the plane above the cells are outlined and faintly fluorescent. (a) The control distribution of PC3 cells flowed through the sample channel without an applied electric field, and (b) PC3 cells experience pDEP under 75 V, 300 kHz.

The devices were not able to sort a mixture of highly aggressive murine ovarian cancer cells (FFLs) with fibroblasts (OP9), as both cell types responded similarly at varied frequencies (Figure 21). However, these cell types have previously been difficult to separate at high frequencies, likely due to their similar sizes (unpublished data), and we posit that sorting these cells requires a sensitive device designed to sort them near their respective crossover frequencies (<100 kHz). In terms of response, they showed comparable results to the PC3 cells, where near 300 kHz short pearl chains were observed, and as the frequency increased toward 500 kHz, cells deflected to the top of the channel and were trapped at the highest frequencies.

(a) (b)

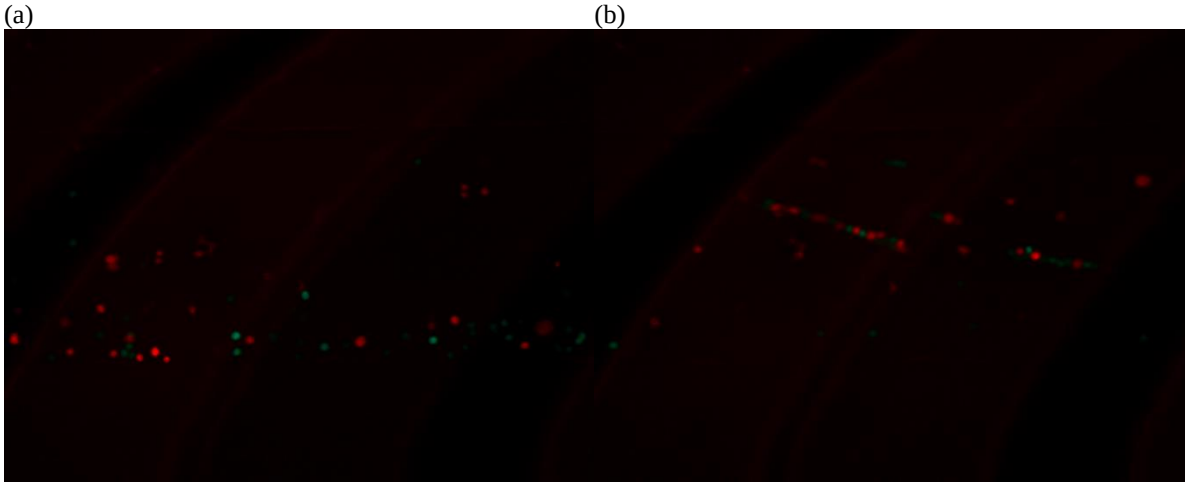

Figure 21. (a) A mixture of murine FFL (green) and OP9 cells (red) were flowed through the device at 0.005 ml/hr without any external field applied. (b) Cells show pearl chaining and are continuously deflected upwards through the channel at 75 V, 300 kHz.

5.4 Future Work

5.4.1 Future Device Design Work

The current work was constrained to using a circular arc shape for the curved electrode channels. However, more drastically curved shapes should be explored to determine the effect on the direction of distinct cell populations. Additionally, electrode channels should be sectioned by including more inlet and outlets to reduce the electrical resistance, which would allow more electrode pairs to be placed in series, increasing separation resolution. While the current design was fabricated with only one layer of electrode channels and was able to demonstrate bulk cell deflection, another layer of electrode channels can be added below the sample channel to allow for deeper sample channels and thus higher throughput, while preventing the deleterious decay of the electric field far from the electrode channels. Also, the current cell sorting devices should be tested with mixture of cells that are more dissimilar than the mixture of FFL and OP9 cells to determine their use for sorting of some cell mixtures. For example, they may prove useful for sorting cancer cells from red blood cells (RBCs) as RBCs are known to be much smaller in size and generally have higher crossover frequencies than mammalian cancer cells.

5.4.2 Potential of cDEP for Drug Screening Applications

Future work will focus on the use of cDEP for screening applications, with specific interest in chemotherapeutic drugs or non-toxic treatments for cancer cells. Specifically to this study of MOSE cells and sphingolipid treatments, cells could be either treated with So or S1P, or left untreated, then blinded for characterization by cDEP, following which the cells could be implanted into an animal for validation of the characterization analysis. The reverse could also be performed; treated or untreated cells implanted into animals could be allowed to grow for a time, after which a biopsy from the area (presumably either a tumor or benign tissue) would be removed for analysis of electrical signature. Further developing robust correlations between electrical properties of cells and their particular disease states will potentially enable cDEP for use as a drug screening method for clinical use, supporting personalized medicine. Samples of cells could be treated with various drugs and varying dosages to rapidly assess their efficacy for a particular patient, to address the detrimental patient-to-patient variable drug response is known to introduce uncertainty into the treatment regimen. Beyond the realm of cancer, this technique shows promise for general use as a drug screening tool for any drug or treatment that targets the cytoskeleton or membrane, and presumably also the size and shape, of a cell affected by other diseases.

Appendix A: Matlab Code for Image Processing

Below is a sample of Matlab code used to plot the relative distribution of cells across the sample channel. This code was used for image processing the experimental data from low-frequency continuous sorting cDEP devices to extract dielectric properties of MOSE cells.

```
function image_analysis(file_name, x_offset,y_offset, threshold)
clc

cell_threshold = 60;
switch nargin
    case 1
        x_offset=0;
        y_offset=0;
    case 2
        y_offset=0;
    case 4
        cell_threshold = threshold
end
%cut line for cell evaluation
         x2 = [450+x_offset,450+x_offset];
         y2 = [150+y_offset, 460+y_offset];
% Read movie file in
        dir = 'C:\ALIREZA FILES\DEP\OVARIAN\Low Freq Movies\MOSE p70+1\';
        read_file = strcat(dir, file_name, '.avi')
%addpath read_file
        path(path,dir)
        movie = mmreader(read_file);
% file_info = aviinfo('control.avi')
        num_frames= movie.NumberOfFrames
%display the first frame and the cut line
        mov(1).cdata = read(movie, 1);
        frame = mov(1).cdata;

        red_frame = frame(:,:, 1);
        red_frame(:,:,2) = 0;
        red_frame(:,:,3) = 0;

        green_frame = frame(:,:, 2);
        green_frame(:,:,2) = 0;
        green_frame(:,:,3) = 0;

        blue_frame = frame(:,:, 3);
        blue_frame(:,:,2) = 0;
        blue_frame(:,:,3) = 0;
```

```
        size(frame)
        size(red_frame)

        A = rgb2gray(frame);
        B = rgb2gray(red_frame);
        C = rgb2gray(green_frame);
        D = rgb2gray(blue_frame);

%plot frame
        figure(1), subplot(2,2,1),imshow(A)
        subplot(2,2,2),imshow(B)
        subplot(2,2,3),imshow(C)
        subplot(2,2,4),imshow(D)
        hold on
%plot data line
        plot (x2,y2,'-rx')
%hold off
        start_frame = 1;
        end_frame =num_frames;
        tic

        distribution = [];
        old_dist = [];          %use this to control the plotting of some data later on

%split movie into individual frames
        for cur_frame = start_frame:5:end_frame - 15
```

```
%movie and frame data
         clear mov;
         mov(cur_frame).cdata = read(movie, cur_frame);
         frame = mov(cur_frame).cdata;
         A = rgb2gray(frame);
%plot frame
            if(mod(cur_frame, 2)==1)
                figure(3), imshow(A);
                hold on
%plot data line
                plot (x2,y2,'-rx')
                hold off
            end
```

```
%original pixal data
            c = improfile(A,x2,y2);
%plot pixel data
            figure(4)
            subplot(4,1,1),title(file_name),plot(c)
            hold on, plot([0 length(c)], [cell_threshold cell_threshold])
            hold off
```

```
%smoothed pixel data
            output = smooth(c, 10);
%             output = smooth(c, 2);              %reduce smooth size to account for
smaller cells

%plot smothed pixel data
            subplot(4,1,2),
          if(mod(cur_frame, 2)==1)
            plot(output, '-r'),
            hold on
            plot([0 length(output)], [cell_threshold cell_threshold]), hold off
          end
%thresholded pixel data
            threshold = output>cell_threshold;
%             threshold = output<cell_threshold;      %threshold value depends on
focusing (this is out of focus)
%             subplot(4,1,3),hold on,
%              plot(threshold, '-b');

            %distribution

            if(size(distribution) == 0)
                distribution = zeros(size(threshold));
                distribution = distribution + threshold;
                old_dist = distribution;
            else
                distribution = distribution + threshold;
            end

            if (distribution == old_dist)
            else
                %if distribution has changed, plot
                %     subplot(4,1,4),
                subplot(2,1,2)
                plot(distribution, '-b');
                title(file_name);
                hold off
                %             pause(.1)
            end

            old_dist = distribution;
```

```
        end

        new_dist=distribution/sum(distribution)*100;
        accum=0;
        i=1;
        while (accum<50)
```

```
            accum=new_dist(i)+accum;
            i=i+1;
        end
            hold off
        toc

        directory = 'output files/';
        file = strcat(directory,file_name, '.mat');
        save(file, 'file_name','i','-mat')

        file = strcat(directory,file_name, '.txt');
        save(file, 'new_dist', '-ascii')

        beep; pause(1);beep;
end
```

Appendix B: Data from Numerical Models

Further data from the numerical modeling and parametric study of the multilayer interdigitated electrode design is provided here. Figure B1 illustrates $\nabla(E \cdot E)$ for the case of 6, 10, and 12 electrode pairs, which were not presented in the body of this work. As previously stated, increasing the number of electrode pairs decreased the potential drop between central source and sink electrode channels. Even at six electrode pairs, sufficient DEP force was not generated for central electrode pairs at frequencies above 200 kHz.

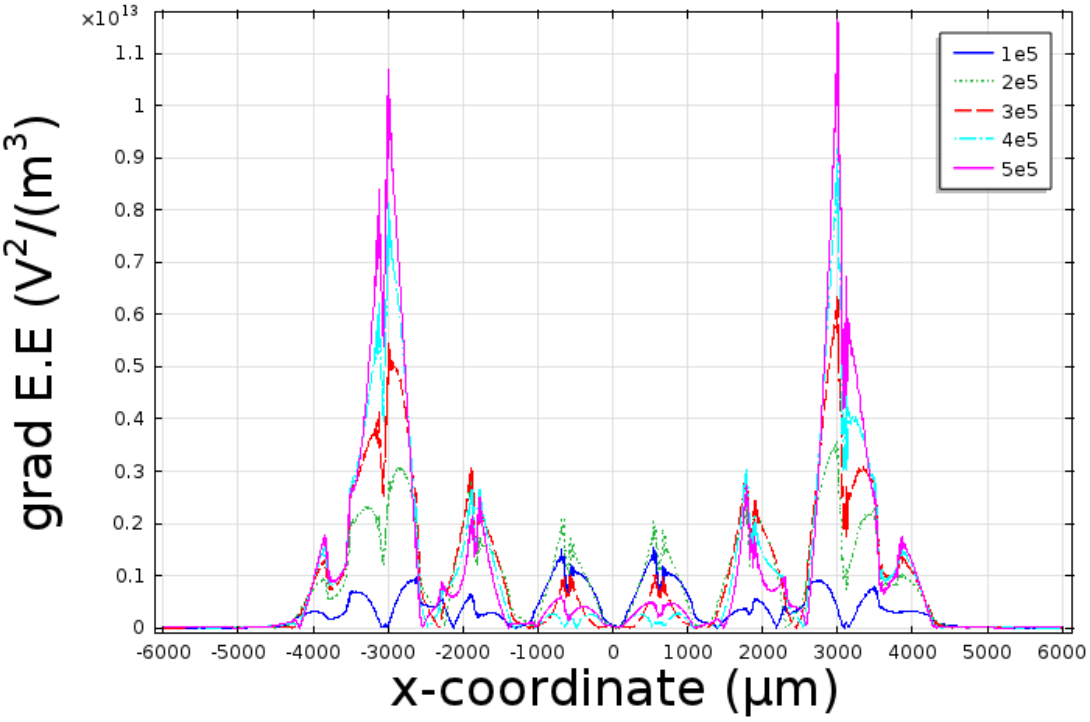

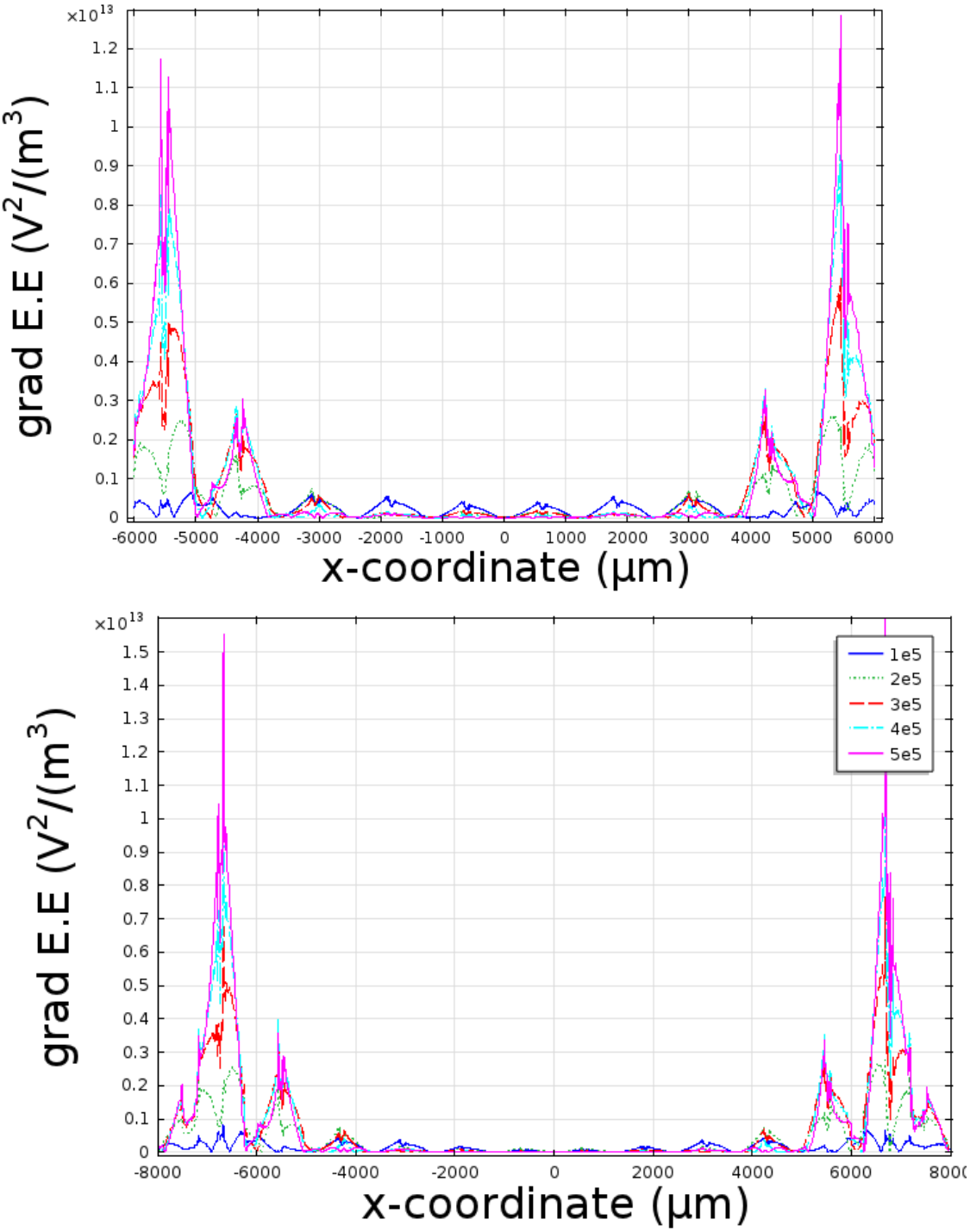

Figure B1. The frequency-dependent solution for $\nabla(E \cdot E)$ was determined along the x-direction at a centerline 15 μm below the sample channel ceiling for (a) 6 electrode pairs, (b) 10 electrode pairs, and (c) 12 electrode pairs. The legends display frequency in units of kHz.

Appendix C: Further Numerical Models of New Designs for cDEP Devices

Beside the multilayer interdigitated curved electrode design presented in the body of the thesis, new low frequency designs were modeled with the goal of generating DEP force across the entire width of the sample channel to ensure that the entire cell distribution is exposed to DEP force. Figure C1 shows a low frequency design with electrode channel spacing and dimensions identical to the device previously presented for low frequency operation, with the exception of the geometric features in the sample channel. In contrast to the previous design, this device has symmetric constrictions rather than asymmetric sawtooth constrictions. It is expected that this device would sort one cell population by pDEP into two streams along the top and bottom of channel and the remaining cell population into a third stream through the center of the channel by nDEP.

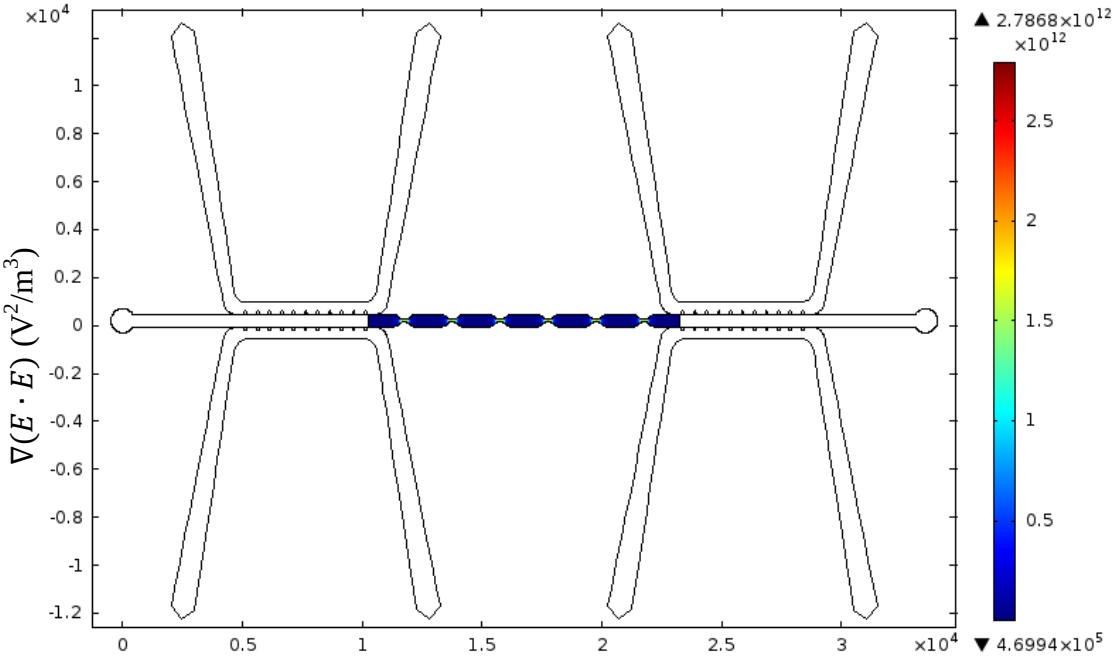

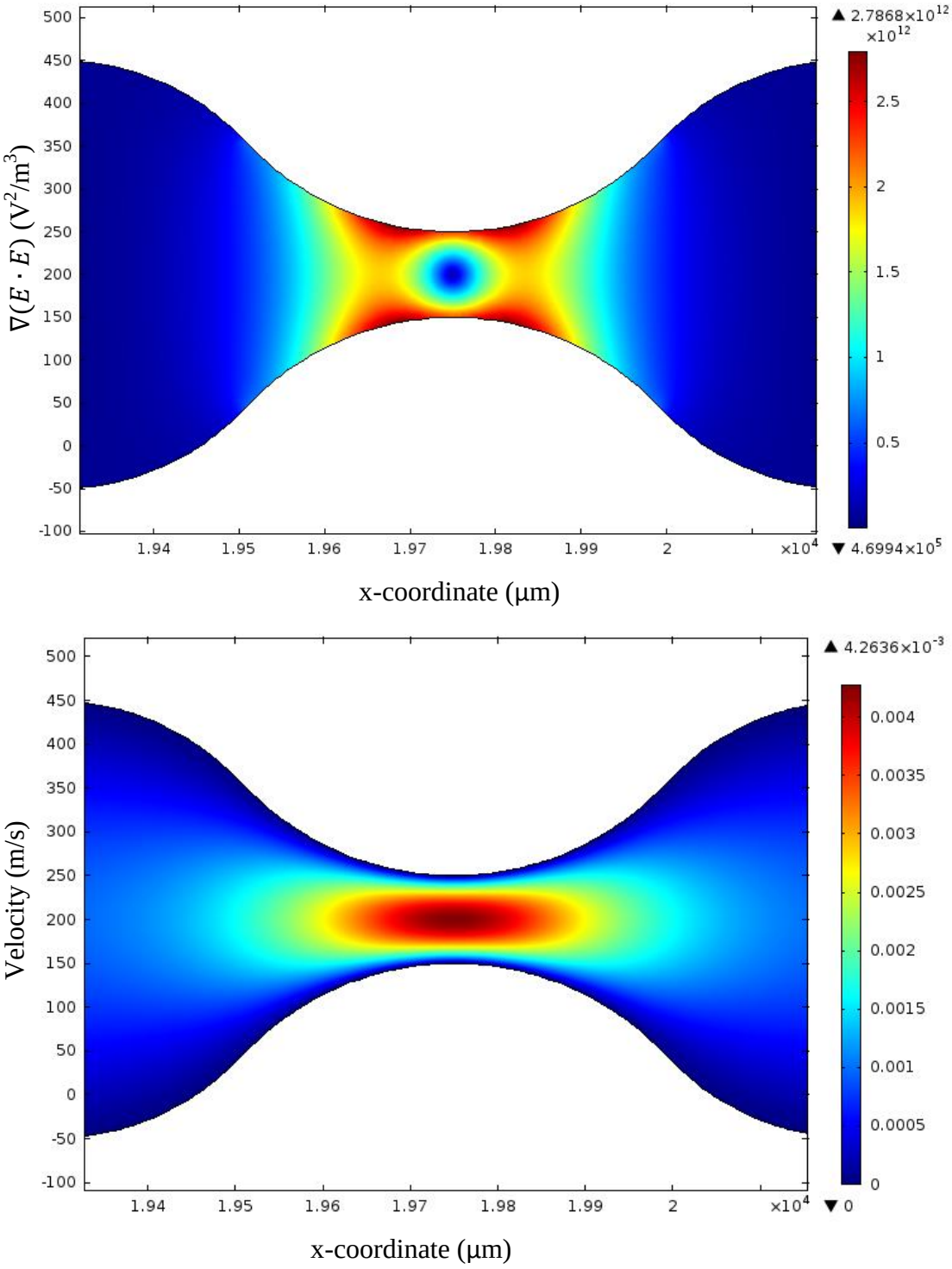

Figure C1. (a) A low frequency device design consisting of symmetric constrictions in series was modeled at 25 kHz. (b) Sufficient $\nabla(E \cdot E)$ to manipulate cell motion was generated in the constrictions of the devices. (c) The velocity of the fluid through the constriction was predicted to be maximal in the constriction.

Additionally, another multilayer design incorporating interdigitated electrodes was numberically modeled (Figure C2). This design is intended to support additional focusing

of sorted particle streams by including zig-zag electrode channels downstream from diagonal electrode channels. According to the numerical modeling, sufficient DEP force should be generated at both sets of electrodes to manipulate cells. Also, the design incorporates multiple inlets to potentially facilitate hydrodynamic sorting and focusing, as the cell mixture can be introduced through the upper channel of the y-inlet, while buffer is introduced in the bottom inlet and the downstream inlet. The cell suspension should be focused at the top of the channel, so cells influenced by the DEP force should be forced down the slanted electrodes to the bottom or middle region of the channel. The high maxima of DEP force at the points of the zig-zag electrode channels should aid in focusing previously sorted cells. This numerical model was an early model solved using a coarse mesh to gain a general prediction of the electric field distribution. For further development, the mesh should be refined and experimental devices tested. Also, the electrode channel design should be altered to one more reminiscent of the presented electrode channels; the early design would be prone to trapped air bubbles when using the devices for experiments.

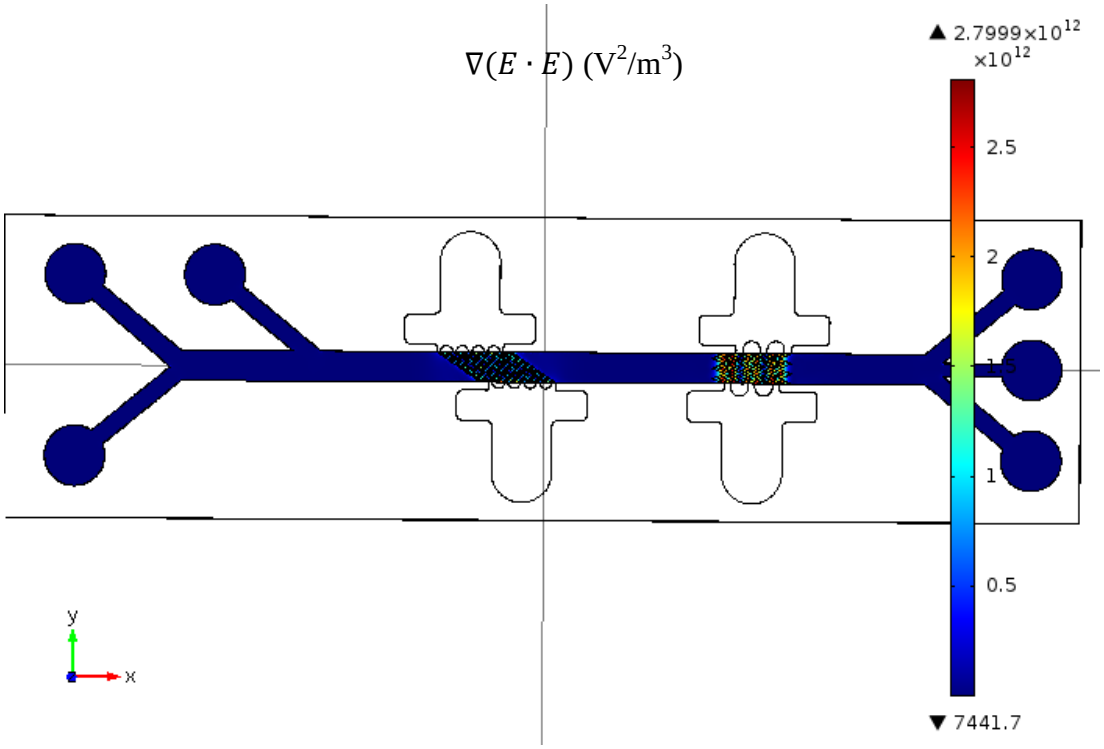

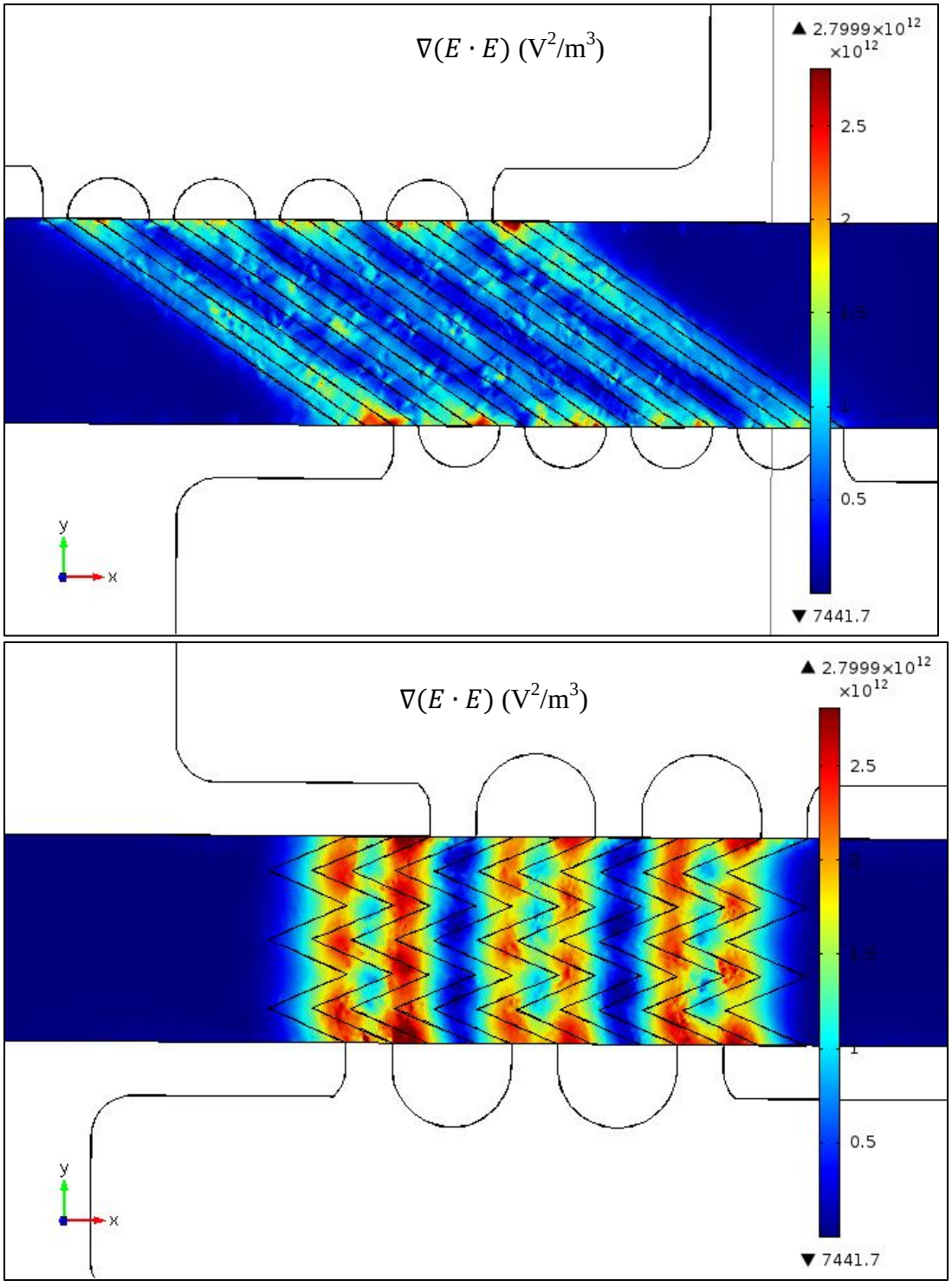

Figure C2 (a) A multilayer cDEP device was numerically modeled to predict $\nabla(E \cdot E)$. By introducing a cell mixture into the top outlet at the y-inlet and buffer into the bottom inlet channel and the downstream inlet channel, hydrodynamic focusing can allow the cell mixture to flow past the top of the slanted electrodes. (b) Slanted interdigitated electrode channels generate DEP force that directs targeted particles to the bottom of the channel to achieve cell sorting. (c) Zig-zag electrode channels generate maxima of DEP force to support focusing of cells previously sorted upstream.

References

[1] N. A. Howlader N, Krapcho M, Garshell J, Neyman N, Altekruse SF, Kosary CL, Yu M, Ruhl J, Tatalovich Z, Cho H, Mariotto A, Lewis DR, Chen HS, Feuer EJ, Cronin KA *SEER Cancer Statistics Review, 1975-2010,* . Available: http://seer.cancer.gov/csr/1975_2010/

[2] N. A. Howlader N, Krapcho M, Neyman N, Aminou R, Waldron W, Altekruse SF, Kosary CL, Ruhl J, Tatalovich Z, Cho H, Mariotto A, Eisner MP, Lewis DR, Chen HS, Feuer EJ, Cronin KA (2012). *SEER Cancer Statistics Review, 1975-2009 (Vintage 2009 Populations)*. Available: http://seer.cancer.gov/csr/1975_2009_pops09/

[3] I. Visintin, Z. Feng, G. Longton, D. C. Ward, A. B. Alvero, Y. Lai, J. Tenthorey, A. Leiser, R. Flores-Saaib, H. Yu, M. Azori, T. Rutherford, P. E. Schwartz, and G. Mor, "Diagnostic markers for early detection of ovarian cancer," *Clin Cancer Res*, vol. 14, pp. 1065-72, Feb 15 2008.

[4] I. J. Jacobs and U. Menon, "Progress and challenges in screening for early detection of ovarian cancer," *Mol Cell Proteomics*, vol. 3, pp. 355-66, Apr 2004.

[5] R. Siegel, D. Naishadham, and A. Jemal, "Cancer statistics, 2013," *CA Cancer J Clin*, vol. 63, pp. 11-30, Jan 2013.

[6] (August 2012). *Cancer Trends Progress Report – 2011/2012 Update*. Available: http://progressreport.cancer.gov.

[7] A. Basu and S. Krishnamurthy, "Cellular responses to Cisplatin-induced DNA damage," *J Nucleic Acids*, vol. 2010, 2010.

[8] C. D. Scripture, W. D. Figg, and A. Sparreboom, "Peripheral neuropathy induced by paclitaxel: recent insights and future perspectives," *Curr Neuropharmacol*, vol. 4, pp. 165-72, Apr 2006.

[9] H. A. Pohl, *Dielectrophoresis : the behavior of neutral matter in nonuniform electric fields*. Cambridge ; New York: Cambridge University Press, 1978.

[10] T. Sun, H. Morgan, and N. G. Green, "Analytical solutions of ac electrokinetics in interdigitated electrode arrays: electric field, dielectrophoretic and traveling-wave dielectrophoretic forces," *Phys Rev E Stat Nonlin Soft Matter Phys*, vol. 76, p. 046610, Oct 2007.

[11] E. M. Schmelz, P. C. Roberts, E. M. Kustin, L. A. Lemonnier, M. C. Sullards, D. L. Dillehay, and A. H. Merrill, Jr., "Modulation of intracellular beta-catenin localization and intestinal tumorigenesis in vivo and in vitro by sphingolipids," *Cancer Res*, vol. 61, pp. 6723-9, Sep 15 2001.

[12] E. M. Schmelz, M. C. Sullards, D. L. Dillehay, and A. H. Merrill, Jr., "Colonic cell proliferation and aberrant crypt foci formation are inhibited by dairy glycosphingolipids in 1, 2-dimethylhydrazine-treated CF1 mice," *J Nutr*, vol. 130, pp. 522-7, Mar 2000.

[13] L. A. Lemonnier, D. L. Dillehay, M. J. Vespremi, J. Abrams, E. Brody, and E. M. Schmelz, "Sphingomyelin in the suppression of colon tumors: prevention versus intervention," *Arch Biochem Biophys*, vol. 419, pp. 129-38, Nov 15 2003.

[14] K. W. Simon, L. Tait, F. Miller, C. Cao, K. P. Davy, T. Leroith, and E. M. Schmelz, "Suppression of breast xenograft growth and progression in nude mice: implications for the use of orally administered sphingolipids as chemopreventive agents against breast cancer," *Food Funct,* vol. 1, pp. 90-8, Jan 10 2010.

[15] J. C. Mazzei, H. Zhou, B. P. Brayfield, R. Hontecillas, J. Bassaganya-Riera, and E. M. Schmelz, "Suppression of intestinal inflammation and inflammation-driven colon cancer in mice by dietary sphingomyelin: importance of peroxisome proliferator-activated receptor gamma expression," *J Nutr Biochem,* Feb 3 2011.

[16] C. R. Gault, L. M. Obeid, and Y. A. Hannun, "An overview of sphingolipid metabolism: from synthesis to breakdown," *Sphingolipids as Signaling and Regulatory Molecules,* vol. 688, pp. 1-23, 2010.

[17] H. Vesper, E. M. Schmelz, M. N. Nikolova-Karakashian, D. L. Dillehay, D. V. Lynch, and A. H. Merrill, Jr., "Sphingolipids in food and the emerging importance of sphingolipids to nutrition," *Journal of Nutrition,* vol. 129, pp. 1239-50, Jul 1999.

[18] P. Gangoiti, L. Camacho, L. Arana, A. Ouro, M. H. Granado, L. Brizuela, J. Casas, G. Fabrias, J. L. Abad, A. Delgado, and A. Gomez-Munoz, "Control of metabolism and signaling of simple bioactive sphingolipids: Implications in disease," *Progress in Lipid Research,* vol. 49, pp. 316-334, Oct 2010.

[19] R. Kolesnick and D. W. Golde, "The Sphingomyelin Pathway in Tumor-Necrosis-Factor and Interleukin-1 Signaling," *Cell,* vol. 77, pp. 325-328, May 6 1994.

[20] R. N. Kolesnick and M. R. Hemer, "Characterization of a Ceramide Kinase-Activity from Human Leukemia (Hl-60) Cells - Separation from Diacylglycerol Kinase-Activity," *Journal of Biological Chemistry,* vol. 265, pp. 18803-18808, Nov 5 1990.

[21] S. Spiegel and S. Milstien, "Sphingosine-1-phosphate: An enigmatic signalling lipid," *Nature Reviews Molecular Cell Biology,* vol. 4, pp. 397-407, May 2003.

[22] M. Maceyka, S. G. Payne, S. Milstien, and S. Spiegel, "Sphingosine kinase, sphingosine-1-phosphate, and apoptosis," *Biochimica Et Biophysica Acta-Molecular and Cell Biology of Lipids,* vol. 1585, pp. 193-201, Dec 30 2002.

[23] C. Chalfant and M. Del Poeta, *Sphingolipids as signaling and regulatory molecules*. New York, N.Y.
Austin, Tex.: Springer Science+Business Media ;
Landes Bioscience, 2010.

[24] V. Teichgraber, M. Ulrich, N. Endlich, J. Riethmuller, B. Wilker, C. C. De Oliveira-Munding, A. M. van Heeckeren, M. L. Barr, G. von Kurthy, K. W. Schmid, M. Weller, B. Tummler, F. Lang, H. Grassme, G. Doring, and E. Gulbins, "Ceramide accumulation mediates inflammation, cell death and infection susceptibility in cystic fibrosis," *Nat Med,* vol. 14, pp. 382-91, Apr 2008.

[25] D. Wang, Z. Zhao, A. Caperell-Grant, G. Yang, S. C. Mok, J. Liu, R. M. Bigsby, and Y. Xu, "S1P differentially regulates migration of human ovarian cancer and human ovarian surface epithelial cells," *Molecular Cancer Therapeutics,* vol. 7, pp. 1993-2002, Jul 2008.

[26] B. Visentin, J. A. Vekich, B. J. Sibbald, A. L. Cavalli, K. M. Moreno, R. G. Matteo, W. A. Garland, Y. L. Lu, S. X. Yu, H. S. Hall, V. Kundra, G. B. Mills, and R. A. Sabbadini, "Validation of an anti-sphingosine-1-phosphate antibody as

a potential therapeutic in reducing growth, invasion, and angiogenesis in multiple tumor lineages," *Cancer Cell,* vol. 9, pp. 225-238, Mar 2006.

[27] P. K. Wong, T. H. Wang, J. H. Deval, and C. M. Ho, "Electrokinetics in micro devices for biotechnology applications," *Ieee-Asme Transactions on Mechatronics,* vol. 9, pp. 366-376, Jun 2004.

[28] H. A. Pohl, "Some Effects of Nonuniform Fields on Dielectrics," *Journal of Applied Physics,* vol. 29, pp. 1182-1188, 1958.

[29] H. A. Pohl, "The Motion and Precipitation of Suspensoids in Divergent Electric Fields," *Journal of Applied Physics,* vol. 22, pp. 869-871, 1951.

[30] H. A. Pohl and I. Hawk, "Separation of living and dead cells by dielectrophoresis," *Science,* vol. 152, pp. 647-9, Apr 29 1966.

[31] H. A. Pohl and J. S. Crane, "Dielectrophoresis of cells," *Biophysical Journal,* vol. 11, pp. 711-27, Sep 1971.

[32] J. S. Crane and H. A. Pohl, "Theoretical models of cellular dielectrophoresis," *Journal of Theoretical Biology,* vol. 37, pp. 15-41, Oct 1972.

[33] R. Martinez-Duarte, "Microfabrication technologies in dielectrophoresis applications-A review," *ELECTROPHORESIS,* vol. 33, pp. 3110-3132, Nov 2012.

[34] L. Cui, D. Holmes, and H. Morgan, "The dielectrophoretic levitation and separation of latex beads in microchips," *ELECTROPHORESIS,* vol. 22, pp. 3893-3901, Oct 2001.

[35] T. Sun, H. Morgan, and N. G. Green, "Analytical solutions of ac electrokinetics in interdigitated electrode arrays: Electric field, dielectrophoretic and traveling-wave dielectrophoretic forces," *Physical Review E,* vol. 76, Oct 2007.

[36] N. G. Green, A. Ramos, and H. Morgan, "Numerical solution of the dielectrophoretic and travelling wave forces for interdigitated electrode arrays using the finite element method," *Journal of Electrostatics,* vol. 56, pp. 235-254, Sep 26 2002.

[37] Y. Hubner, K. F. Hoettges, G. E. N. Kass, S. L. Ogin, and M. P. Hughes, "Parallel measurements of drug actions on Erythrocytes by dielectrophoresis, using a three-dimensional electrode design," *IEEE Proceedings-Nanobiotechnology,* vol. 152, pp. 150-154, Aug 2005.

[38] M. Cristofanilli, G. De Gasperis, L. Zhang, M. C. Hung, P. R. Gascoyne, and G. N. Hortobagyi, "Automated electrorotation to reveal dielectric variations related to HER-2/neu overexpression in MCF-7 sublines," *Clinical Cancer Research,* vol. 8, pp. 615-9, Feb 2002.

[39] M. Desmond, N. Mavrogiannis, and Z. Gagnon, "Maxwell-Wagner Polarization and Frequency-Dependent Injection at Aqueous Electrical Interfaces," *Phys Rev Lett,* vol. 109, Oct 31 2012.

[40] T. B. Jones, "Liquid dielectrophoresis on the microscale," *Journal of Electrostatics,* vol. 51, pp. 290-299, May 2001.

[41] E. D. Pratt, C. Huang, B. G. Hawkins, J. P. Gleghorn, and B. J. Kirby, "Rare Cell Capture in Microfluidic Devices," *Chem Eng Sci,* vol. 66, pp. 1508-1522, Apr 1 2011.

[42] A. Salmanzadeh and R. V. Davalos, "Isolation of rare cells through their dielectrophoretic signature," *Journal of Membrane Science and Technology,* pp. under-review, 2012.
[43] R. Pethig and G. H. Markx, "Applications of dielectrophoresis in biotechnology," *Trends in Biotechnology,* vol. 15, pp. 426-432, Oct 1997.
[44] R. Pethig, "Dielectrophoresis: Status of the theory, technology, and applications (vol 4, 022811, 2010)," *Biomicrofluidics,* vol. 4, Sep 2010.
[45] P. R. C. Gascoyne, J. V. Vykoukal, J. A. Schwartz, T. J. Anderson, D. M. Vykoukal, K. W. Current, C. McConaghy, F. F. Becker, and C. Andrews, "Dielectrophoresis-based programmable fluidic processors," *Lab on a Chip,* vol. 4, pp. 299-309, 2004.
[46] L. A. Flanagan, J. Lu, L. Wang, S. A. Marchenko, N. L. Jeon, A. P. Lee, and E. S. Monuki, "Unique dielectric properties distinguish stem cells and their differentiated progeny," *Stem Cells,* vol. 26, pp. 656-665, 2008.
[47] R. Pethig, "Cell Physiometry Tools based on Dielectrophoresis," in *BioMEMS and Biomedical Nanotechnology*, M. Ferrari, M. Ozkan, and M. Heller, Eds., ed: Springer US, 2007, pp. 103-126.
[48] R. Pethig, A. Menachery, S. Pells, and P. De Sousa, "Dielectrophoresis: A Review of Applications for Stem Cell Research," *Journal of Biomedicine and Biotechnology,* 2010.
[49] M. P. Hughes, H. Morgan, and F. J. Rixon, "Measuring the dielectric properties of herpes simplex virus type 1 virions with dielectrophoresis," *Biochimica Et Biophysica Acta-General Subjects,* vol. 1571, pp. 1-8, May 10 2002.
[50] G. H. Markx, M. S. Talary, and R. Pethig, "Separation of Viable and Nonviable Yeast Using Dielectrophoresis," *Journal of Biotechnology,* vol. 32, pp. 29-37, Jan 15 1994.
[51] H. S. Moon, K. Kwon, S. I. Kim, H. Han, J. Sohn, S. Lee, and H. I. Jung, "Continuous separation of breast cancer cells from blood samples using multi-orifice flow fractionation (MOFF) and dielectrophoresis (DEP)," *Lab on a Chip,* vol. 11, pp. 1118-1125, 2011.
[52] R. Pethig, "Dielectrophoresis: Using inhomogeneous AC electrical fields to separate and manipulate cells," *Critical Reviews in Biotechnology,* vol. 16, pp. 331-348, 1996.
[53] F. H. Labeed, H. M. Coley, H. Thomas, and M. P. Hughes, "Assessment of multidrug resistance reversal using dielectrophoresis and flow cytometry," *Biophysical Journal,* vol. 85, pp. 2028-2034, Sep 2003.
[54] K. F. Hoettges, Y. Hubner, L. M. Broche, S. L. Ogin, G. E. N. Kass, and M. P. Hughes, "Dielectrophoresis-activated multiwell plate for label-free high-throughput drug assessment," *Analytical Chemistry,* vol. 80, pp. 2063-2068, Mar 15 2008.
[55] L. C. Hsiung, C. L. Chiang, C. H. Wang, Y. H. Huang, C. T. Kuo, J. Y. Cheng, C. H. Lin, V. Wu, H. Y. Chou, D. S. Jong, H. Lee, and A. M. Wo, "Dielectrophoresis-based cellular microarray chip for anticancer drug screening in perfusion microenvironments," *Lab Chip,* vol. 11, pp. 2333-2342, 2011.
[56] H. M. Coley, F. H. Labeed, H. Thomas, and M. P. Hughes, "Biophysical characterization of MDR breast cancer cell lines reveals the cytoplasm is critical

in determining drug sensitivity," *Biochimica et Biophysica Acta,* vol. 1770, pp. 601-608, Apr 2007.

[57] K. Khoshmanesh, J. Akagi, S. Nahavandi, J. Skommer, S. Baratchi, J. M. Cooper, K. Kalantar-Zadeh, D. E. Williams, and D. Wlodkowic, "Dynamic Analysis of Drug-Induced Cytotoxicity Using Chip-Based Dielectrophoretic Cell Immobilization Technology," *Analytical Chemistry,* vol. 83, pp. 2133-2144, Mar 15 2011.

[58] R. Pethig, V. Bressler, C. Carswell-Crumpton, Y. Chen, L. Foster-Haje, M. E. Garcia-Ojeda, R. S. Lee, G. M. Lock, M. S. Talary, and K. M. Tate, "Dielectrophoretic studies of the activation of human T lymphocytes using a newly developed cell profiling system," *ELECTROPHORESIS,* vol. 23, pp. 2057-2063, Jul 2002.

[59] R. Pethig, "Biological Electrostatics - Dielectrophoresis and Electrorotation," *Institute of Physics Conference Series,* pp. 13-26, 1991.

[60] B. H. Lapizco-Encinas, B. A. Simmons, E. B. Cummings, and Y. Fintschenko, "Insulator-based dielectrophoresis for the selective concentration and separation of live bacteria in water," *ELECTROPHORESIS,* vol. 25, pp. 1695-1704, Jun 2004.

[61] S. Masuda, T. Itagaki, and M. Kosakada, "Detection of Extremely Small Particles in the Nanometer and Ionic Size Range," *Ieee Transactions on Industry Applications,* vol. 24, pp. 740-744, Jul-Aug 1988.

[62] S.-W. Lee, Y. Sung-Dong, K. Yong-Wook, K. Yong-Kweon, and L. Sang-Hoon, "Micromachined cell handling devices," in *Engineering in Medicine and Biology Society, 1994. Engineering Advances: New Opportunities for Biomedical Engineers. Proceedings of the 16th Annual International Conference of the IEEE*, 1994, pp. 1019-1020 vol.2.

[63] E. B. Cummings and A. K. Singh, "Dielectrophoresis in microchips containing arrays of insulating posts: Theoretical and experimental results," *Analytical Chemistry,* vol. 75, pp. 4724-4731, Sep 15 2003.

[64] B. H. Lapizco-Encinas, B. A. Simmons, E. B. Cummings, and Y. Fintschenko, "Dielectrophoretic concentration and separation of live and dead bacteria in an array of insulators," *Analytical Chemistry,* vol. 76, pp. 1571-1579, Mar 15 2004.

[65] B. H. Lapizco-Encinas, R. V. Davalos, B. A. Simmons, E. B. Cummings, and Y. Fintschenko, "An insulator-based (electrodeless) dielectrophoretic concentrator for microbes in water," *Journal of Microbiological Methods,* vol. 62, pp. 317-326, Sep 2005.

[66] B. A. Simmons, B. Lapizco-Encinas, G. J. Fiechtner, E. B. Cummings, Y. Fintschenko, R. Shediac, J. Hachman, and J. M. Chames, "Polymeric insulating post electrodeless dielectrophoresis (EDEP) for the monitoring of water-borne pathogens," *Abstracts of Papers of the American Chemical Society,* vol. 227, pp. U464-U465, Mar 28 2004.

[67] R. V. Davalos, G. J. McGraw, T. I. Wallow, A. M. Morales, K. L. Krafcik, Y. Fintschenko, E. B. Cummings, and B. A. Simmons, "Performance impact of dynamic surface coatings on polymeric insulator-based dielectrophoretic particle separators," *Analytical and Bioanalytical Chemistry,* vol. 390, pp. 847-55, Feb 2008.

[68] R. C. Gallo-Villanueva, C. E. Rodriguez-Lopez, R. I. Diaz-De-La-Garza, C. Reyes-Betanzo, and B. H. Lapizco-Encinas, "DNA manipulation by means of insulator-based dielectrophoresis employing direct current electric fields," *ELECTROPHORESIS,* vol. 30, pp. 4195-4205, Dec 2009.

[69] R. Martinez-Duarte, P. Renaud, and M. J. Madou, "A novel approach to dielectrophoresis using carbon electrodes," *ELECTROPHORESIS,* vol. 32, pp. 2385-2392, Sep 2011.

[70] H. Shafiee, J. L. Caldwell, M. B. Sano, and R. V. Davalos, "Contactless dielectrophoresis: a new technique for cell manipulation," *Biomedical Microdevices,* vol. 11, pp. 997-1006, Oct 2009.

[71] K. Park, H. J. Suk, D. Akin, and R. Bashir, "Dielectrophoresis-based cell manipulation using electrodes on a reusable printed circuit board," *Lab on a Chip,* vol. 9, pp. 2224-2229, 2009.

[72] C. P. Jen, N. A. Maslov, H. Y. Shih, Y. C. Lee, and F. B. Hsiao, "Particle focusing in a contactless dielectrophoretic microfluidic chip with insulating structures," *Microsystem Technologies-Micro-and Nanosystems-Information Storage and Processing Systems,* vol. 18, pp. 1879-1886, Nov 2012.

[73] H. Shafiee, M. B. Sano, E. A. Henslee, J. L. Caldwell, and R. V. Davalos, "Selective isolation of live/dead cells using contactless dielectrophoresis (cDEP)," *Lab on a Chip,* vol. 10, pp. 438-45, Feb 21 2010.

[74] E. A. Henslee, M. B. Sano, A. D. Rojas, E. M. Schmelz, and R. V. Davalos, "Selective concentration of human cancer cells using contactless dielectrophoresis," *ELECTROPHORESIS,* vol. 32, pp. 2523-9, Sep 2011.

[75] M. B. Sano, J. L. Caldwell, and R. V. Davalos, "Modeling and development of a low frequency contactless dielectrophoresis (cDEP) platform to sort cancer cells from dilute whole blood samples," *Biosensors & Bioelectronics,* vol. 30, pp. 13-20, Dec 15 2011.

[76] A. Salmanzadeh, M. B. Sano, R. C. Gallo-Villanueva, P. C. Roberts, E. M. Schmelz, and R. V. Davalos, "Investigating dielectric properties of different stages of syngeneic murine ovarian cancer cells," *Biomicrofluidics,* vol. 7, p. 011809, 2013.

[77] M. B. Sano, E. A. Henslee, E. Schmelz, and R. V. Davalos, "Contactless dielectrophoretic spectroscopy: Examination of the dielectric properties of cells found in blood," *ELECTROPHORESIS,* vol. 32, pp. 3164-3171, Nov 2011.

[78] Y. H. Zhan, Z. N. Cao, N. Bao, J. B. Li, J. Wang, T. Geng, H. Lin, and C. Lu, "Low-frequency ac electroporation shows strong frequency dependence and yields comparable transfection results to dc electroporation," *Journal of Controlled Release,* vol. 160, pp. 570-576, Jun 28 2012.

[79] M. B. Sano, A. Salmanzadeh, and R. V. Davalos, "Multilayer contactless dielectrophoresis: Theoretical considerations," *ELECTROPHORESIS,* vol. 33, pp. 1938-1946, 2012.

[80] M. Danova, M. Torchio, and G. Mazzini, "Isolation of rare circulating tumor cells in cancer patients: technical aspects and clinical implications," *Expert Rev Mol Diagn,* vol. 11, pp. 473-85, Jun 2011.

[81] M. Chabert and J. L. Viovy, "Microfluidic high-throughput encapsulation and hydrodynamic self-sorting of single cells," *Proceedings of the National Academy of Sciences of the United States of America,* vol. 105, pp. 3191-3196, Mar 4 2008.
[82] D. Di Carlo, D. Irimia, R. G. Tompkins, and M. Toner, "Continuous inertial focusing, ordering, and separation of particles in microchannels," *Proc Natl Acad Sci U S A,* vol. 104, pp. 18892-7, Nov 27 2007.
[83] D. Di Carlo, "Inertial microfluidics," *Lab on a Chip,* vol. 9, pp. 3038-46, Nov 7 2009.
[84] H. Tsutsui and C. M. Ho, "Cell separation by non-inertial force fields in microfluidic systems," *Mechanics Research Communications,* vol. 36, pp. 92-103, Jan 2009.
[85] S. C. Grover, A. G. Skirtach, R. C. Gauthier, and C. P. Grover, "Automated single-cell sorting system based on optical trapping," *Journal of Biomedical Optics,* vol. 6, pp. 14-22, Jan 2001.
[86] D. G. Grier, "A revolution in optical manipulation," *Nature,* vol. 424, pp. 810-816, Aug 14 2003.
[87] S. C. S. Lin, X. L. Mao, and T. J. Huang, "Surface acoustic wave (SAW) acoustophoresis: now and beyond," *Lab on a Chip,* vol. 12, pp. 2766-2770, 2012.
[88] R. Pethig, "Review Article-Dielectrophoresis: Status of the theory, technology, and applications," *Biomicrofluidics,* vol. 4, Jun 2010.
[89] P. R. C. Gascoyne, X. B. Wang, Y. Huang, and F. F. Becker, "Dielectrophoretic separation of cancer cells from blood," *Ieee Transactions on Industry Applications,* vol. 33, pp. 670-678, May-Jun 1997.
[90] P. R. C. Gascoyne, Y. Huang, X. J. Wang, J. Yang, G. DeGasperis, and X. B. Wang, "Cell separation by conventional dielectrophoresis combined with field-flow-fractionation," *Biophysical Journal,* vol. 70, pp. Tu412-Tu412, Feb 1996.
[91] M. Wiklund, C. Gunther, R. Lemor, M. Jager, G. Fuhr, and H. M. Hertz, "Ultrasonic standing wave manipulation technology integrated into a dielectrophoretic chip," *Lab on a Chip,* vol. 6, pp. 1537-1544, Dec 2006.
[92] W. A. Bonner, H. R. Hulett, R. G. Sweet, and L. A. Herzenberg, "Fluorescence activated cell sorting," *Rev Sci Instrum,* vol. 43, pp. 404-9, Mar 1972.
[93] J. D. Adams, U. Kim, and H. T. Soh, "Multitarget magnetic activated cell sorter," *Proceedings of the National Academy of Sciences of the United States of America,* vol. 105, pp. 18165-18170, Nov 25 2008.
[94] I. Safarik and M. Safarikova, "Use of magnetic techniques for the isolation of cells," *Journal of Chromatography B,* vol. 722, pp. 33-53, Feb 5 1999.
[95] J. J. Chalmers, M. Zborowski, L. P. Sun, and L. Moore, "Flow through, immunomagnetic cell separation," *Biotechnology Progress,* vol. 14, pp. 141-148, Jan-Feb 1998.
[96] S. F. Ibrahim and G. van den Engh, "High-speed cell sorting: fundamentals and recent advances," *Current Opinion in Biotechnology,* vol. 14, pp. 5-12, Feb 2003.
[97] M. Stephens, M. S. Talary, R. Pethig, A. K. Burnett, and K. I. Mills, "The dielectrophoresis enrichment of CD34(+) cells from peripheral blood stem cell harvests," *Bone Marrow Transplantation,* vol. 18, pp. 777-782, Oct 1996.

[98] S. Shim, P. Gascoyne, J. Noshari, and K. S. Hale, "Dynamic physical properties of dissociated tumor cells revealed by dielectrophoretic field-flow fractionation," *Integrative Biology*, vol. 3, pp. 850-862, 2011.
[99] H. Morgan, T. Sun, D. Holmes, S. Gawad, and N. G. Green, "Single cell dielectric spectroscopy," *Journal of Physics D-Applied Physics*, vol. 40, pp. 61-70, Jan 7 2007.
[100] R. S. Thomas, H. Morgan, and N. G. Green, "Negative DEP traps for single cell immobilisation," *Lab on a Chip*, vol. 9, pp. 1534-1540, 2009.
[101] A. Menachery, D. Graham, S. M. Messerli, R. Pethig, and P. J. S. Smith, "Dielectrophoretic tweezer for isolating and manipulating target cells," *Iet Nanobiotechnology*, vol. 5, pp. 1-7, Mar 2011.
[102] Z. R. Gagnon, "Cellular dielectrophoresis: applications to the characterization, manipulation, separation and patterning of cells," *ELECTROPHORESIS*, vol. 32, pp. 2466-87, Sep 2011.
[103] P. R. Gascoyne and J. V. Vykoukal, "Dielectrophoresis-Based Sample Handling in General-Purpose Programmable Diagnostic Instruments," *Proc IEEE Inst Electr Electron Eng*, vol. 92, pp. 22-42, Jan 1 2004.
[104] M. B. Sano, E. A. Henslee, E. Schmelz, and R. V. Davalos, "Contactless dielectrophoretic spectroscopy: examination of the dielectric properties of cells found in blood," *ELECTROPHORESIS*, vol. 32, pp. 3164-71, Nov 2011.
[105] A. Salmanzadeh, L. Romero, H. Shafiee, R. C. Gallo-Villanueva, M. A. Stremler, S. D. Cramer, and R. V. Davalos, "Isolation of prostate tumor initiating cells (TICs) through their dielectrophoretic signature," *Lab on a Chip*, vol. 12, pp. 182-9, Jan 7 2012.
[106] A. Salmanzadeh, H. Kittur, M. B. Sano, C. R. P, E. M. Schmelz, and R. V. Davalos, "Dielectrophoretic differentiation of mouse ovarian surface epithelial cells, macrophages, and fibroblasts using contactless dielectrophoresis," *Biomicrofluidics*, vol. 6, pp. 24104-2410413, Jun 2012.
[107] P. C. Roberts, E. P. Mottillo, A. C. Baxa, H. H. Heng, N. Doyon-Reale, L. Gregoire, W. D. Lancaster, R. Rabah, and E. M. Schmelz, "Sequential molecular and cellular events during neoplastic progression: a mouse syngeneic ovarian cancer model," *Neoplasia*, vol. 7, pp. 944-56, Oct 2005.
[108] A. L. Creekmore, W. T. Silkworth, D. Cimini, R. V. Jensen, P. C. Roberts, and E. M. Schmelz, "Changes in gene expression and cellular architecture in an ovarian cancer progression model," *PLoS One*, vol. 6, 2011.
[109] A. N. Ketene, P. C. Roberts, A. A. Shea, E. M. Schmelz, and M. Agah, "Actin filaments play a primary role for structural integrity and viscoelastic response in cells," *Integrative Biology*, vol. 4, pp. 540-549, 2012.
[110] T. M. Squires and S. R. Quake, "Microfluidics: Fluid physics at the nanoliter scale," *Reviews of Modern Physics*, vol. 77, pp. 977-1026, Jul 2005.
[111] T. B. Jones, *Electromechanics of particles*. Cambridge ; New York: Cambridge University Press, 1995.
[112] U. Segar, "Electrical cell manipulation
in microfluidic systems," ÉCOLE POLYTECHNIQUE FÉDÉRALE DE LAUSANNE, 2006.

[113] T. B. Jones, "Basic theory of dielectrophoresis and electrorotation," *Ieee Engineering in Medicine and Biology Magazine*, vol. 22, pp. 33-42, Nov-Dec 2003.
[114] H. G. a. G. Morgan, N., Ed., *Electrokinetic technologies for sub-micron particles* (Microtechnologies and Microsystems. Hertfordshire, England: Research Studies Press, Ltd., 2003, p.^pp. Pages.
[115] H. G. Morgan, N.G., Ed., *Electrokinetic technologies for sub-micron particles* (Microtechnologies and Microsystems. Hertfordshire, England: Research Studies Press Ltd., 2003, p.^pp. Pages.
[116] T. B. Jones, "Dielectrophoretic Force Calculation," *Journal of Electrostatics*, vol. 6, pp. 69-82, 1979.
[117] A. Salmanzadeh, E. S. Elvington, P. C. Roberts, E. M. Schmelz, and R. V. Davalos, "Sphingolipid metabolites modulate dielectric characteristics of cells in a mouse ovarian cancer progression model," *Integr Biol (Camb)*, Apr 23 2013.
[118] A. N. Ketene, E. M. Schmelz, P. C. Roberts, and M. Agah, "The effects of cancer progression on the viscoelasticity of ovarian cell cytoskeleton structures (vol 8, pg 93, 2012)," *Nanomedicine-Nanotechnology Biology and Medicine*, vol. 8, pp. 391-391, Apr 2012.
[119] H. Babahosseini, P. C. Roberts, E. M. Schmelz, and M. Agah, "Roles of bioactive sphingolipid metabolites in ovarian cancer cell biomechanics," *Conf Proc IEEE Eng Med Biol Soc*, vol. 2012, pp. 2436-9, 2012.